

Advances in Dynamic Light Scattering Imaging of Blood Flow

Anton Sdobnov, Gennadii Piavchenko, Alexander Bykov, and Igor Meglinski*

Dynamic light scattering (DLS) is a well known experimental approach uniquely suited for the characterization of small particles undergoing Brownian motion in randomly inhomogeneous turbid scattering medium, including water suspension, polymers in solutions, cells cultures, and so on. DLS is based on the illuminating of turbid medium with a coherent laser light and further analyzes the intensity fluctuations caused by the motion of the scattering particles. The DLS-based spin-off derivative techniques, such as laser Doppler flowmetry (LDF), diffusing wave spectroscopy (DWS), laser speckle contrast imaging (LSCI), and Doppler optical coherence tomography (DOCT), are exploited widely for non-invasive imaging of blood flow in brain, skin, muscles, and other biological tissues. The recent advancements in the DLS-based imaging technologies in frame of their application for brain blood flow monitoring, skin perfusion measurements, and non-invasive blood micro-circulation characterization are overviewed. The fundamentals, breakthrough potential, and practical findings revealed by DLS-based blood flow imaging studies, including the limitations and challenges of the approach such as movement artifacts, non-ergodicity, and overcoming high scattering properties of studied medium, are also discussed. It is concluded that continued research and further technological advancements in DLS-based imaging will pave the way for new exciting developments and insights into blood flow diagnostic imaging.

1. Introduction

The dynamic light scattering (DLS) approach is based on the photons' correlation and statistical analysis of the intensity fluctuations of laser light that appeared due to scattering on moving particles in the studied specimen.^[1] While the velocity of moving particles is relatively slow compared to the speed of light, the amount of Doppler shift is minuscule compared to the frequency of light. Therefore, in line with photon correlation velocimetry^[2] and laser Doppler flowmetry (LDF),^[3] the definition of quasi-elastic light scattering is typically used to describe the current approach.^[4,5] The detection of intensity fluctuations in scattered light is performed by counting the individual photons; hence, the name of photon correlation spectroscopy (PCS) has been widely employed elsewhere.^[2,6,7] The technique is also known as light-beating or intensity-fluctuation spectroscopy, as the "beating" of light intensity is actually analyzed.^[6,8]


First announced in 1955 by Forrester^[9] and then confirmed by Brown and Twiss^[10] the light-beating spectroscopy was quite limited for practical diagnostic applications due to the broad spectrum and low intensity of the available light sources at that time. With the advent of the lasers, which provided high spectral purity, the DLS approach became a popular diagnostic tool.^[11] In 1964, Cummins et al. reported the use of lasers as a source for investigation of diffusion spectrum broadening for the Rayleigh scattering on the monodisperse polystyrene molecules.^[11]

In 1972 Riva et al. demonstrated the applicability of LDF for measurements of blood flow in the retinal arteries as well as whole blood flowing through capillary tubes.^[12] Three years later, Stern pioneered the LDF measurements of blood microcirculation on the finger.^[13] He also reported observation of the pulsatile component in the Doppler system and studied the responses of the blood perfusion of outer cortex of the rat kidney to various drugs.^[14] Holloway and Watkins designed the fiber-probe LDF system suitable for clinical applications and validated the approach with the washout technique.^[15] Later, Bonner and Nassal introduced the theoretical background of LDF for blood flow measurements.^[16] Later a number of various commercial

A. Sdobnov, A. Bykov, I. Meglinski
Optoelectronics and Measurement Techniques
University of Oulu
Oulu 90570, Finland
E-mail: i.meglinski@aston.ac.uk

G. Piavchenko, I. Meglinski
Department of Histology, Cytology and Embryology
Institute of Clinical Medicine N.V. Sklifosovsky
I.M. Sechenov First Moscow State Medical University
8-2 Trubetskaya str., Moscow 119991, Russia

I. Meglinski
College of Engineering and Physical Sciences
Aston University
Birmingham B4 7ET, UK

 The ORCID identification number(s) for the author(s) of this article can be found under <https://doi.org/10.1002/lpor.202300494>

© 2023 The Authors. Laser & Photonics Reviews published by Wiley-VCH GmbH. This is an open access article under the terms of the Creative Commons Attribution License, which permits use, distribution and reproduction in any medium, provided the original work is properly cited.

DOI: 10.1002/lpor.202300494

LDF-based systems were introduced for biomedical applications and pre-clinical studies.^[17]

Studies of both intensity fluctuations and Doppler shifted linewidths of light scattered by human skin have been reported utilizing PCS.^[18] In the late 1980s, the DLS approach has been extended to the media characterized by strong multiple scattering of laser light, since that was known as a diffusing wave spectroscopy (DWS).^[19,20] After numerous comprehensive theoretical and instrumentation practice studies^[21–25] the DWS has been successfully implemented for non-invasive monitoring and measurements of the parameters of blood flow,^[26,27] burn depth estimation,^[28] pre-clinical studies of blood samples in vitro,^[29] brain blood flow functional diagnosis and vasculature imaging,^[30,31] assessment of cancerous tissues during photodynamic therapy,^[32] skin blood perfusion monitoring,^[33,34] assessment of kidney blood flow,^[35] atherosclerotic disease diagnosis,^[36] and others. Subsequent developments of the DWS approach employing near-infrared light for non-invasive measurement, with a focus on directly measuring local microvascular cerebral blood flow (CBF), are also collectively known as diffuse correlation spectroscopy (DCS).^[37,38] Among the DLS, LDF, and DWS, there is also a full-field method known as speckle imaging or laser speckle contrast imaging (LSCI).^[39,40] Introduced in 1981^[39] the LSCI utilizes a coherent laser source (e.g., a laser diode) for illumination of object of interest and a digital camera (CCD or CMOS) for raw speckle image acquisition and is extensively used in various pre-clinical examinations for monitoring of blood microcirculation in the superficial layers of biological tissues, for example, for screening blood flow in tumors.^[41] LSCI is a simple, cost-effective, and powerful method based on statistical analysis of speckle patterns arising as a result of coherent light interaction with a randomly inhomogeneous medium.^[42]

LSCI-based systems have been successfully implemented in various biomedical applications, including cerebral blood flow monitoring,^[43] in vivo characterization of tumors and tumor vascular networks,^[41] ophthalmology,^[44] and clinical use on skin.^[45] There are several commercially available LSCI devices widely used for clinical applications.^[46,47] LSCI is also effectively used for non-biological applications such as surface roughness evaluation,^[48,49] evaluation of handwriting peculiarities,^[50] paint drying monitoring,^[51] and others.

Doppler-based approach was further combined with the optical coherence tomography (OCT),^[52] and the resultant Doppler optical coherence tomography (DOCT) allows simultaneous acquisition of high-resolution structural images and flow velocity measurements,^[53,54] including flow dynamics in complex vessels.^[55–57] DOCT has been successfully used for cerebral blood flow monitoring,^[58,59] retinal imaging.^[60] A combined use of DLS and OCT approaches provides an opportunity for 3D visualization of flows in biological tissue,^[61,62] whereas the implementation of 4D echocardiography allows simultaneous tissue and blood flow Doppler imaging.^[63]

A survey benchmark comparison of the DLS-based spin-off derivative techniques mentioned above with other imaging modalities utilized for non-invasive imaging of blood flows and blood microcirculation in terms of spatial and temporal resolution, penetration depth, and scattering regime is presented in **Figure 1**.

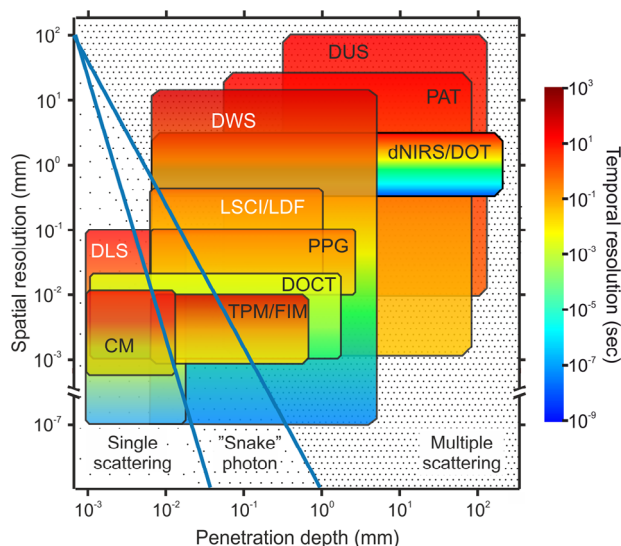


Figure 1. Major imaging diagnostic modalities utilized for non-invasive imaging and characterization of blood flow compared by spatial and temporal resolution, penetration depth, and regime of scattering. Here, dNIRS, diffuse near-infrared spectroscopy; DOT, diffuse optical tomography; DWS, diffusing wave spectroscopy; DLS, dynamic light scattering; LSCI, laser speckle contrast imaging; LDF, laser Doppler flowmetry; DOCT, Doppler optical coherence tomography; PAT, photo-acoustic tomography; CM, confocal microscopy; DUS, Doppler ultra-sound. DLS-based techniques are colored white.

Other techniques presented in Figure 1 in comparison to DLS and DLS-based spin-off derivative techniques are photoplethysmography (PPG),^[64] fluorescence intravital microscopy (FIM),^[65,66] diffuse near-infrared spectroscopy (dNIRS),^[67] photo-acoustic tomography (PAT),^[68,69] Doppler ultra-sound (DUS),^[70] diffuse optical tomography (DOT),^[71] confocal microscopy (CM),^[72] and two-photon microscopy (TPM),^[73] are also implemented for the blood flow diagnosis.^[74]

In the current review, we focus on the recent advances in DLS-based imaging modalities and discuss the breakthrough potential of non-invasive imaging and the characterization of blood flow and blood microcirculation.

2. Basics of the Dynamic Light Scattering

2.1. Temporal Intensity Auto-Correlation

In DLS-based blood flow imaging approaches (**Figure 2**), the primary measure obtained experimentally is the time-dependent intensity fluctuations of light scattered within the biological tissue. The intensity fluctuations arise from changes in the constructive or destructive interference of the scattered waves due to the displacement of scattering particles, for example, red blood cells (RBC) within the tissues. The rate of recorded intensity fluctuations caused by the motion of the scatterers is quantitatively characterized by the temporal intensity auto-correlation function^[19,21]

$$g_2(\tau) = \frac{\langle I(t)I(t+\tau) \rangle}{\langle I(t) \rangle^2} \quad (1)$$

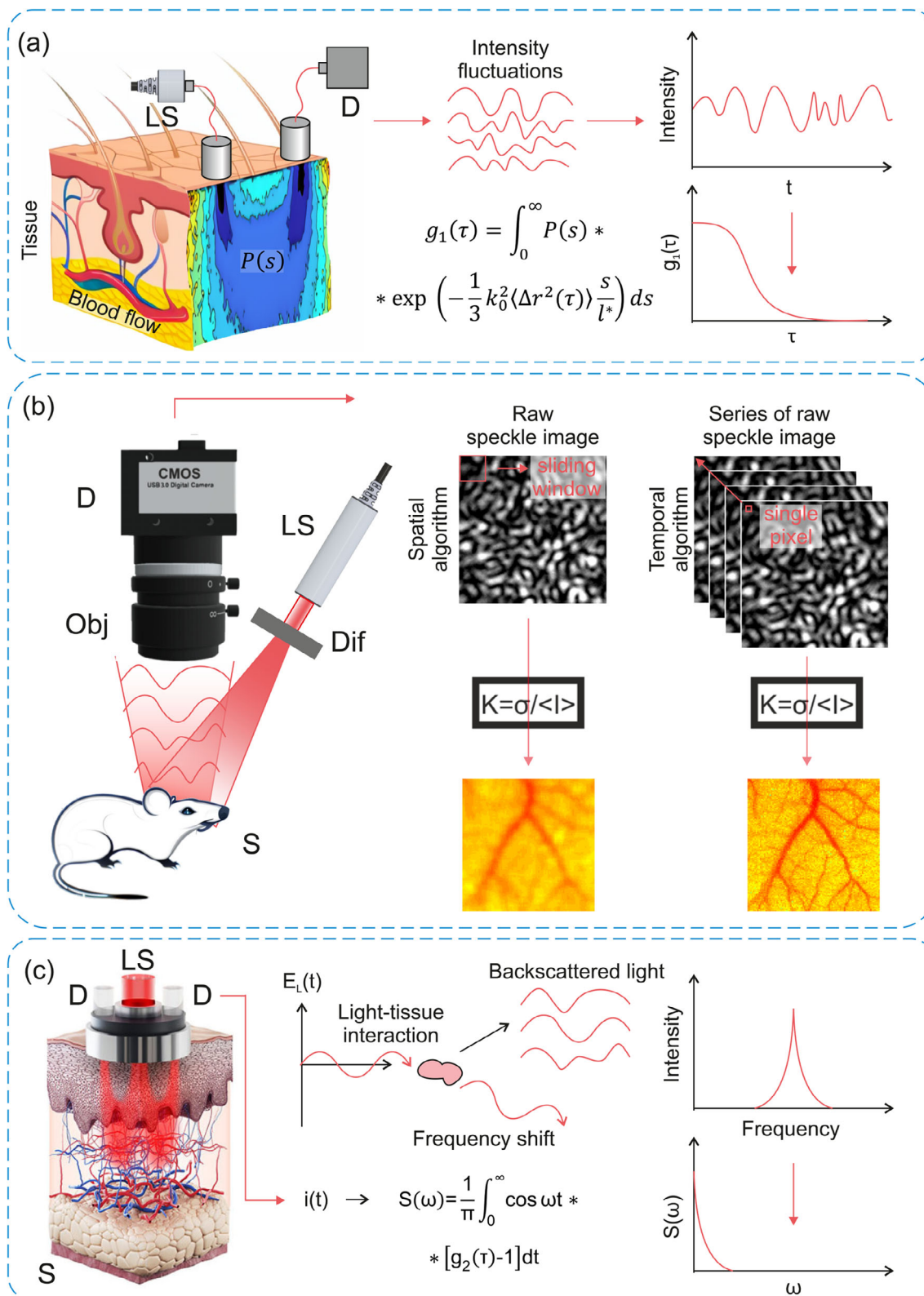


Figure 2. Schematic presentations of typical DLS-based experimental approaches and principles of data processing utilized for blood flow imaging, including: a) DWS (here, $P(s)$ defines the distribution of photon trajectories s within the medium between light source LS and detector D, $k_0 = \frac{2\pi n}{\lambda}$, n is the refractive index of the medium, λ is the wavelength, and l^* is the transport mean free path of scattered light); b) LSCI; and c) LDF. Here, LS, light source; D, detector/camera; Dif, diffuser; Obj, objective; and S, sample. Adapted with permission under terms of the CC BY 4.0 license.^[144] Copyright 2023, The Authors, published by IEEE.

where $I(t)$ and $I(t + \tau)$ are the measured intensities of scattered light at the instants of time t and $t + \tau$, respectively, the angular brackets $\langle \dots \rangle$ denotes averaging on time, and τ is the time delay. While the key measure in DLS is the time-dependent intensity fluctuations of light scattered by biological tissue, the interpretation of the results involves analyzing the underlying fluctuations in terms of electric field. The temporal intensity fluctuations of scattered light are related to the fluctuations in the electric field through the concept of coherence. More specifically, the temporal field autocorrelation function ($g_1(\tau)$) describes the temporal coherence properties of the electric field of the scattered light^[75]

$$g_1(\tau) = \frac{\langle E(t)E^*(t + \tau) \rangle}{\langle E(t) \cdot E^*(t) \rangle} \quad (2)$$

where $E(t)$ is the electric field of detected light, $E^*(t)$ is the complex conjugate of the electric field. $g_1(\tau)$ represents the correlation of the electric field at different time points. In the context of light scattering, $g_1(\tau)$ and $g_2(\tau)$ are related through the Siegert relation^[4,76]

$$g_2(\tau) = 1 + \beta |g_1(\tau)|^2 \quad (3)$$

where β is the distribution parameter that can be conceptually grasped as the relative measurement-geometry specific contrast, or the degree of coherence of the detected signal, or the “intercept” of the correlogram.^[77,78] It represents the degrees of freedom, which in DLS, correspond to the number of independent speckles within the detector aperture. Therefore, also known as an aperture function,^[79] it is contingent upon a characteristic of the optical configuration within the actual DLS experimental setup, particularly in the context of the collection optics. Importantly, this parameter is not linked to the dynamics of the scattering particles; rather, it pertains to the polarization properties of light, coherence, and the mismatch between the image pixel size and the speckle size at the digital camera.^[78,80,81] It should be emphasized that the spatial coherence properties of the used light influence mainly the size of the formed speckles, also it is shown that the speckle contrast value is linearly proportional to the temporal coherence value.^[82,83]

Siegert’s relation (Equation (3)) holds for the fully coherent light scattering, where $g_1(\tau)$ is complex-valued, and the $g_2(\tau)$ is real-valued. Importantly, this relation allows us to directly define $g_1(\tau)$ from the measured $g_2(\tau)$. This provides an opportunity to analyze the temporal coherence properties of the scattered laser light based on the observed intensity fluctuations. In addition, Siegert’s relation becomes especially valuable when employed in conjunction with the Wiener–Khinchine theorem, as it establishes a direct connection between the spectral width of light and the correlation time of intensity fluctuations.

Under the assumption of ergodicity $g_2(\tau)$ describes the correlation between the intensity fluctuation values at different time delays and is used to extract information about particle size, diffusion coefficient,^[84] and/or dynamic properties of the scattering medium, for example, such as, velocity of scattering particles in flow.^[25] The diffusion coefficient (D) is a key parameter derived from the ensemble scattering measurements. It quantifies the average speed of particles undergoing Brownian motion^[84] and

provides information about the size and dynamics of the scatterers

$$D = \frac{k_B T}{6\pi\eta r} \quad (4)$$

Here, k_B is the Boltzmann constant, T is the temperature, η is the dynamic viscosity, and r is the radius of the scattering particle. The diffusion coefficient is defined directly through the analysis of $g_2(\tau)$ and related to the hydrodynamic radius of the particles using the Einstein–Stokes relation.^[84] The decay rate of $g_2(\tau)$ is referred to as the correlation time (τ), provides a measure of the characteristic time scale of scattering. It is related to the average time it takes for the intensity fluctuations to decorrelate. In the DLS-based approach the decay rate ($\Gamma = -\ln|g_1(\tau)|$) is used to estimate the diffusion coefficient, as $\Gamma \propto \frac{1}{6}q^2 \langle \Delta r^2(\tau) \rangle$, where q is the scattering vector ($q = k_f - k_o$, k_o and k_f are the incident and scattered wave vectors, respectively) and $\langle \Delta r^2(\tau) \rangle$ is the mean-square displacement of the scattering particles.

DLS is indeed based on the principles of Brownian motion and light scattering to analyze the size and diffusion properties of particles in a sample: $\langle \Delta r^2(\tau) \rangle = 6D\tau$. In fact, the high sensitivity of multiple-scattering speckle patterns to the movement of scattering particles has given rise to a new methodology termed DWS.^[19,20] DWS has been extended for the investigation of macroscopically heterogeneous turbid media (see Figure 2a), offering a valuable tool for imaging dynamic variations and visualizing the flows of scattering entities within the bulk of the medium.^[25,85,86] In the case of flow, unlike Brownian motion, $\langle \Delta r^2(\tau) \rangle \approx \tau^2$. This holds true for the observation of shear, Poiseuille flow, and plug flow of non-Newtonian fluids.^[86–89]

Last decade, the methods based on the time-domain signal analysis, utilizing $g_2(\tau)$, obtained a reasonable acceptance in the soft matter community, where they are used for the high precision quantitative particle sizing and characterization of complex media.^[90] Furthermore, it has been tailored to analyze non-ergodic turbid media,^[91,92] thereby expanding its applicability in the study of various intricate living systems.^[26–28,31,93] Thus, extended for use in turbid dynamic media, such as biological tissues, where a diffusive regime of light scattering is assumed, DLS, known as DWS and/or DSC (see Figure 2a), applied extensively for blood flow diagnosis.^[34,37,38]

2.2. Laser Speckle Contrast

In a typical LSCI experiment (Figure 2b), the intensity fluctuations are detected by optical fiber and/or by pixels at the photodetector (CCD or CMOS camera). Therefore, the signal at the point detector (optical fiber or a pixel) consists of a superposition of a multitude of amplitude spread functions, each arising from different sequences of scattering events that occurred within the scattering medium/biological tissue. The formed point spread functions exhibit markedly different phases, resulting in a random interference pattern known as a laser speckle pattern (see Figure 2b). The theory of speckle pattern formation is comprehensively described by Goodman.^[94] Laser speckles are defined as a random interference pattern arising from the interaction of

the coherent light with a rough surface and with the turbid, randomly inhomogeneous scattering medium. The variations in local dynamics of the medium (e.g., flowing of scattering particles) lead to flickering of speckle patterns and, thus, result in their blurring on the captured frame due to limited camera exposure time. The faster displacement of scattering particles provides a more blurred speckle pattern captured by pixels/camera. This blurring consequently decreases the speckle contrast value (K), which, in fact, allows the quantification of the flow rate.

The laser speckle contrast K is introduced as^[95]

$$K = \sigma / \langle I \rangle \quad (5)$$

and takes values $0 \leq K \leq 1$. Here, σ is the standard deviation and $\langle I \rangle$ is the mean intensity of the detected light. Fercher and Briers showed relation between speckle contrast value, camera exposure time, and speckle correlation time (τ) via theory of correlation functions,^[39] which is widely used in DLS.^[6,7,96] K is related to the autocorrelation function as

$$K(T) = \left[\frac{2\beta}{T} \int_0^T \left| \frac{g_1(\tau)}{g_1(0)} \right|^2 \left(1 - \frac{\tau}{T} \right) d\tau \right]^{1/2} \quad (6)$$

where $K(T)$ is the speckle contrast as the function of the digital camera exposure time T . Fercher and Briers assumed that β coefficient is equal to 1.^[39] Later, taken into account since the reduced variance of the intensity at each pixel of digital camera, Bandyopadhyay showed that β coefficient relates to the $g_1(\tau)$.^[76] It was further accepted that $1/K^2$ is an approximate estimation of T/τ .^[97–102] The hypothetical relation between the speckle correlation time and velocity of scattering particles is defined as^[42,80,103]

$$v \propto \frac{1}{\tau} \quad (7)$$

where v is the velocity of scattering particles. Respectively, $1/K^2$ is showing quantitatively the velocity of flowing scattering particles.^[80] The typical correlation time for DLS-based methods varies from 10^{-6} to 10^{-1} s.^[104,105]

2.3. Sliding Window and Nyquist Criteria

To obtain a spatially resolved measure of the speckle pattern dynamics the sliding window of pixels is used for the raw speckle image processing and speckle contrast ($K(x, y)$) calculation. By using a sliding window,^[42,106–109] the speckle contrast can be calculated locally, providing spatially resolved information about the dynamics within different regions on the obtained image (spatial algorithm). This helps to capture localized changes in the speckle pattern, which may be indicative of different phenomena or physiological processes occurring in biological tissues. Besides, by using a sliding window, the speckle contrast can be calculated for multiple time points within the window, allowing for temporal averaging. This helps to improve the signal-to-noise ratio by reducing the impact of short-term fluctuations or noise, resulting in a more robust measure of the speckle pattern dynamics. The size of the sliding window can be adjusted to match the desired spatial resolution or the characteristics of the speckle pattern being analyzed. Larger window sizes can provide a more global view

of the speckle dynamics, while smaller window sizes allow for more localized analysis. This flexibility allows tailoring the analysis to specific needs and optimize the sensitivity to the dynamic flow variations within the biological tissues under investigation. Phenomenologically, it has been found that the sliding window with the sizes of 5×5 and 7×7 pixels are the most appropriate for speckle contrast calculation.^[42,106,108,109] It was also suggested that for the proper calculations the mean speckle size should satisfy the Nyquist criteria.^[110]

The Nyquist criteria states that in order to accurately represent a signal, the sampling rate should be at least twice the highest frequency present in the signal. In the context of LSCI, the speckle pattern can be considered as a signal with spatial frequency components related to the speckle size. To capture the speckle pattern accurately, the sampling rate (pixel size) should be smaller than half the size of the smallest speckles. By satisfying the Nyquist criteria, the speckle contrast measurement can achieve higher resolution and accuracy, capturing the fine details of the speckle pattern.^[111]

A quite a few studies utilize the 1 pixel to 1 speckle ratio for the DLS-based laser speckle measurements,^[112–114] demonstrating that the mean speckle size influences the spatial resolution and signal-to-noise ratio (SNR) of the LSCI system.^[115] SNR is the dynamic range of speckle contrast values. As it was mentioned before, speckle contrast takes values $0 \leq K \leq 1$. However, in practice the range of calculated speckle contrast values is much smaller. The undersampling of the speckle pattern causes small speckles to be incorrectly represented, resulting in inaccurate estimation of K distribution and interpretation of the results. It also brings a loss of high-frequency information in the speckle pattern, resulting small-scale variations and fine details in the speckle contrast can be smoothed or averaged out. This can lead to an underestimation or blurring of the true speckle contrast values. Therefore, ensuring that the mean speckle size satisfies the Nyquist criteria in laser speckle contrast measurement is crucial to accurately capture and represent the speckle pattern. By satisfying the Nyquist criteria, aliasing effects are minimized, and the spatial resolution and accuracy of the speckle contrast measurement are optimized. Aliasing is a phenomenon where high-frequency information in the signal is improperly represented, leading to induce artificial structures in the speckle pattern that do not exist in the original scene, and/or influence the measured speckle size that may become differ from the true speckle size. These false structures arise due to the incorrect representation of high-frequency components of the speckle pattern. The aliasing-based artifacts are misleading and potentially interfere with accuracy and interpretation of the speckle contrast measurements. Alternatively, the temporal statistical analysis (temporal algorithm) has been introduced for speckle contrast calculation.^[109] The temporal analysis is based on the registration of several consecutive speckle images and further calculation of the speckle contrast value for each specific pixel of the obtaining sequence in time domain. Thus, the described method allows to preserve the initial spatial resolution in exchange to the low temporal resolution. In this way, the tradeoff between spatial and temporal resolution should be taken into account during the measurements. Also, both methods of speckle contrast calculation can be combined in spatio-temporal sampling method where the choice of parameters for speckle contrast calculation is based on the need of high

temporal or spatial resolution.^[116–118] Temporal sampling methods employ broad-spectrum detectors to analyze light signals for sample dynamics. Speckle ensemble methods utilize high-pixel-count cameras to infer dynamics from speckle patterns. Both methods share a unified expression for decorrelation time (τ) accuracy and SNR, based on observables and photon flux.^[119] Recently, the new speckle contrast calculation method has been proposed to preserve both high spatial and temporal resolution in LSCI.^[120]

2.4. Ergodicity

It should be pointed out that in Equation (3) it is generally assumed that the scattering medium or tissue under study satisfies ergodic conditions. Ergodicity is an important concept in the context of relation of $g_2(\tau)$ with $g_1(\tau)$, particularly in the DLS-based experiments. When the ergodicity conditions are met, the statistical properties derived from ensemble scattering ($g_1(\tau)$) and time-averaged measurements ($g_2(\tau)$) are expected to be equivalent. Ergodic conditions are fulfilled if the intensity of light scattered within the probing medium averaged along exposure time (T)^[94]

$$\langle I \rangle = \lim_{T \rightarrow \infty} \frac{1}{T} \int_{-\frac{T}{2}}^{\frac{T}{2}} I(r, t) dt \quad (8)$$

is equal to the intensity of scattered light averaged across an ensemble

$$\langle I \rangle = \int_{-\infty}^{+\infty} I(r, t) P(r) dr \quad (9)$$

Here, $P(r)$ is the probability density function of light intensity $I(r, t)$ observed at pixel $r(x, y)$ on the detector.

In fact, the majority of biological tissues are the highly heterogeneous media, composing mixture of static and dynamic structural inclusions. Due to a displacement Δr of red blood cells (RBC), the time t required for the scattered light to travel along the entire optical path l in the static medium becomes shorter compare to the time ($t + \tau$) in the dynamic medium. As a result, the laser speckles^[94] originating from moving scattering particles are experienced to have intensity fluctuations over the exposure time T in comparison to those arising from static scattering particles. Owing to these intensity fluctuations, this “time-varying” speckle pattern stays correlated for a much shorter period of time τ when compared to the “static” one. Therefore, the statistical properties of laser speckles for the turbid medium with varied moving and static inclusions, as well as the intensities averaged on time (Equation (8)) and ensemble-averaged (Equation (9)), become notably different,^[121] that induces systematic error to the typical DLS-based approaches. Nevertheless, the DLS-based modalities are widely used for blood flow imaging in complex highly heterogeneous biological tissues with multiple static and dynamic scattering inclusions, while the issues associated with the ergodicity are simply ignored.

The classical speckle contrast theory does not consider the possible presence of static (non-ergodic) inclusions. Nevertheless, if scattering object is fully static, the electric field does not change in

time and K value reduces to β . The presence of non-ergodic component produces systematic error in speckle contrast value calculation, which leads to misinterpretation of obtained data.^[81,122–124] Biological tissues consist of both dynamic and static components, such as the skull and skin. Therefore, the issue of non-ergodicity is critical for DLS-based techniques.

In brief, when a digital camera detects light consisting of both dynamic component $E_d(t)$ and static component E_s , the effective electrical field can be represented as^[28,125]

$$E(t) = E_d(t) + E_s \quad (10)$$

In this case, the field autocorrelation function can be rewritten as

$$g_1(\tau) = (1 - \rho) |g_{1d}(\tau)| + \rho \quad (11)$$

where $\rho = I_s / (I_d + I_s)$ is the part of the detected light scattered at the static scattering particles. Further, the intensity autocorrelation function becomes

$$g_2(\tau) = 1 + \beta [(1 - \rho) |g_{1d}(\tau)| + \rho g_1(0)]^2 \quad (12)$$

and speckle contrast becomes

$$K(T) = \left[\frac{2\beta}{T} \int_0^T \left[\frac{(1 - \rho) |g_{1d}(\tau)| + \rho g_1(0)}{g_1(0)} \right]^2 \left(1 - \frac{\tau}{T} \right) d\tau \right]^{1/2} \quad (13)$$

In case of fully dynamic medium, Equation (13) simplifies to Equation (6) due to the absence of any static scatterers ($\rho \rightarrow 0$). However, in the case of a fully static medium, Equation (13) does not reduce to a constant speckle contrast value, as it can be expected for the speckle contrast represented by Equation (9). It is important to notice, that some authors define parameter ρ as the fraction of dynamically scattered light ($\rho \rightarrow 0$ corresponds to the absence of dynamic scatterers).^[126–129]

To address the challenge of non-ergodicity in highly scattering turbid media, various approaches have been developed, including the brute-force method combined with Monte Carlo modeling, multi-exposure speckle imaging, and spatial frequency domain imaging.^[122,128,130] Experimental procedures, such as the slow rotation of a diffuser in the imaging system,^[131] the gradual rotation of the sample itself,^[132] or the introduction of a cell filled with dynamic material placed behind the sample,^[133] are employed to mitigate non-ergodicity. These procedures serve to randomize and gently perturb the speckle pattern of the non-ergodic sample.

It is essential to exercise precision and caution when employing the terms “ergodicity” and “non-ergodicity” in scientific discourse. In a broader theoretical context, ergodicity assumes observations of a medium over an infinitely long duration. However, in practical experiments, the temporal extent of a single measurement is confined by the camera’s exposure time. Consequently, each raw image captured by the camera corresponds to an average signal acquired during this finite exposure interval.

Furthermore, it is noteworthy that, in the majority of cases, the camera’s exposure time significantly exceeds the relaxation time of the dynamic component of the speckle pattern but remains substantially shorter than that of the static component. Under these conditions, the classification of the observed medium as

either ergodic or non-ergodic depends on the specific camera exposure duration employed. For instance, in the general sense, a process characterized by very slow flow is considered ergodic due to the convergence of spatial and temporal statistics over an infinitely long observation period. Nonetheless, the utilization of an imaging system with an exceedingly brief exposure time can result in statistical characteristics resembling those of a non-ergodic process.^[96] Thus, the determination of the influence of ergodic and non-ergodic components on the results of speckle contrast measurements can be a complex task. In contrast, in DWS, the fluctuations due to sample dynamics are easily separated from the ensemble-averaging fluctuations.^[28] Whereas, in the context of LDFs, non-ergodicity can result in inconsistent or fluctuating blood flow readings, making it challenging to obtain accurate and reliable measurements. This is particularly important when blood flow can vary due to physiological or pathological factors.

In the recent study by Sdobnov et al.,^[121] a simple method for estimating speckle dynamics and assessing the impact of non-ergodic components on speckle processing results under specific imaging system parameters was examined. In fully ergodic scattering media, spatial and temporal speckle contrast calculations yield equal results. Conversely, for fully non-ergodic media, temporal and spatial statistics diverge. In the case of a fully developed ideal static speckle pattern, the spatial algorithm yields a theoretical speckle contrast value of 1, as dark and bright speckles correspond to minimal and maximal intensity values, resulting in a standard deviation equal to the mean intensity. In contrast, temporal processing yields a speckle contrast value of 0, as the standard deviation across the image sequence tends to 0 for a fully developed ideal static speckle pattern. However, for dynamic speckle patterns, the speckle contrast value calculated through temporal processing exceeds zero due to an increasing standard deviation. While achieving ideal speckle patterns in experiments is challenging, the disparity between spatial and temporal processing can still be significant.

Further, the authors explored the boundaries of DLS/LSCI applicability when the ergodicity condition is not met.^[134] Through experiments involving phantoms containing intralipid solutions in the presence of static layers with varying thicknesses, coupled with subsequent sampling volume calculations using Monte Carlo simulations, they inferred that the existence of a thick layer of static scatterers above the dynamic layer should not significantly impact the outcomes of spatial and temporal speckle contrast processing. This inference was subsequently validated during transcranial visualization of mouse brain vasculature. The typical thickness of a 2-month-old mouse skull is from 150, to 310 μm .^[135,136] Utilizing an infrared light source offers the advantage of greater probing depth, ensuring that the presence of a static scattering layer (such as the skull) does not adversely affect the quality of blood flow measurements in the mouse brain. Nevertheless, the removal of the skin remains a necessary step. Additionally, the authors demonstrated that the number of frames employed in processing can impact the calculation of spatial and temporal speckle contrast values. Consequently, it was proposed that LSCI/DLS-based imaging system parameters, including exposure time, processing methodology, and the quantity of frames utilized, should be selected with consideration for the experimental objectives to mitigate non-ergodic contributions in measure-

ments. The study also provides a phenomenological rationale for confirming instances in which the DLS-based imaging approach falls short in achieving accurate quantitative transcranial monitoring of blood flow in the brain under conditions characterized by disrupted ergodicity.

2.5. Laser Doppler Flowmetry

LDF is primarily used to measure blood flow in biological tissues. It relies on the Doppler effect, which occurs when light is scattered by flowing RBC within the vessels. The frequency shift of the scattered light is proportional to the velocity of the moving erythrocytes. LDF measures the fluctuating frequency of the scattered light to determine the blood flow velocity and provide information about tissue perfusion. While LDF and DLS share some similarities, they are distinct methods with different measurement objectives. In fact, both techniques utilize the analysis of scattered light to extract information about the motion of the scattering particles. Some studies have explored the combined use of LDF and DLS-based approaches,^[137] where LDF is used to measure blood flow velocity and a DLS-based approach is employed to assess microvascular perfusion. The Winer–Khinchin theorem establishes a mathematical relationship between LDF and DLS. This theorem relates power spectrum ($S(w)$) and $g_2(\tau)$ in the wide-sense stationarity. Thus, $S(w)$ is equally well employed for the analysis of $g_2(\tau)$ since both are related via a Fourier transformation^[6,8]

$$S(w) = \frac{\langle I \rangle}{\pi} \int_{-\infty}^{+\infty} \cos wt [g_2(\tau) - 1] dt \quad (14)$$

The power spectrum ($S(w)$) provides a frequency-domain representation of the signal, and the autocorrelation function ($g_2(\tau)$) provides a time-domain representation. By analyzing the power spectrum, which represents the distribution of frequency components in the scattered light, it was found that the first moment of the spectrum ($S(w)$) provides information about the mean velocity ($\langle V \rangle$) of RBC (scattering particles) in the flow,^[138,139] which is proportional to correlation time ($\propto 1/\tau$). In LDF, the first moment of the power spectrum is not directly related to the mean velocity of the scattering particles. It represents the frequency distribution of the Doppler-shifted light due to the motion of RBC in biological tissues, whereas the mean frequency w^* is velocity-dependent^[16]

$$w^* = \frac{\int_0^{\infty} w S(w) dw}{\int_0^{\infty} S(w) dw} \propto \langle V \rangle \quad (15)$$

In other words, LDF can only capture information about the average velocity and is unable to reveal specifics about the velocity distribution. The typical LDF scheme for blood flow detection and principles of data acquisition are presented in Figure 2c. It is worth noting that the relationship between the first moment of the power spectrum and mean velocity is not specific to LDF alone but can be applicable to various systems involving Doppler measurements, including laser Doppler velocimetry (LDV) and other velocity-sensitive techniques.

2.6. Limitations

Despite the fact that DLS-based spin-off derivative techniques, that is LSCI, LDF, and DWS, are widely exploited for non-invasive diagnosis and imaging of blood flow in various biological tissues,^[140] these modalities are still suffering from imperative drawbacks that impede their transfer to routine day-to-day clinical practice. The major one is the inability to obtain a quantitative link between the measured data and the real physiological parameters of blood flow. Typically, DLS-based approaches provide an average value of blood flow measured over the area illuminated by the laser beam. The spatial resolution is relatively limited, and it is quite challenging to differentiate blood flow changes within small, localized regions. The majority of DLS-based experimental studies of blood flow present relative units instead of absolute values. The serious issue is also the spatial and temporal variability of the DLS-based measuring signal, related to the non-stationary blood flow because of breath, heartbeat, and various complex dynamic processes in biological tissues themselves. DLS-based approaches are limited in their ability to assess deep tissue blood flow accurately. The penetration depth is typically a few millimeters, making it less suitable for assessing blood flow in deeper structures. The spatial variability is usually related to the small sampling volume of the optical fiber probes (within $\approx 1 \text{ mm}^3$ ^[141,142]), which is affected by the local structure of the vasculature and the relative amount of Doppler-shifted photons in the signal.^[143]

The interpretation of DLS-based blood flow measurements can be complicated. The measured values are influenced by a combination of factors, such as tissue scattering properties, probe placement, and local tissue characteristics. The blood flow measurements can be affected by various factors, including skin temperature,^[142] pressure on the probe,^[144] movement artifacts,^[145] and even blood pulsations.^[146] Additionally, individual variations in tissue characteristics, such as pigmentation^[147] or variation in thickness of tissue^[104,148,149] introduce variability in the measurements.

Proper calibration of DLS-based instruments is crucial for obtaining accurate and comparable measurements. Calibration typically involves using standardized flow phantoms,^[125,150] which adds an extra step and complexity to the measurement process. Establishing a baseline measurement helps standardize the assessment of blood flow across different individuals or experimental conditions. It provides a consistent starting point for evaluating the effects of various interventions or stimuli. The uncertainty in the definition of so-called “biological zero” in DLS-based blood flow measurements^[151] serves as a critical point for assessing and interpreting changes in blood flow, providing a standardized baseline for comparison and quantification. In a clinical setting, comparing blood flow measurements to the biological zero can aid in diagnosing and monitoring conditions that affect microcirculation.

The soft biological tissues are highly heterogeneous, composing a mixture of static and dynamic structural inclusions. Due to a displacement of RBC, the time t required for the scattered light to travel along the entire optical path in the static medium becomes shorter compared to the time $(t + \tau)$ in the dynamic medium. As a result, the laser speckles originating from light scattering on moving/displacing particles are experienced to have intensity

fluctuations over the exposure time T in comparison to those arising from static scattering particles. Owing to these intensity fluctuations, this “time-varying” speckle pattern stays correlated for a much shorter period of time τ when compared to the “static” one. Therefore, the statistical properties of laser speckles for the turbid medium with varied moving and static inclusions, as well as the intensities averaged on time (Equation (8)) and ensemble-averaged (Equation (9)), become notably different,^[152] which induces systematic error to the typical DLS approach. The classical DLS approach does not consider the presence of static (non-ergodic) particles. If the scattering medium (tissue) is fully static, the electric field does not change in time and K value reduces to β , see Equation (6). The presence of non-ergodic component produces systematic error during the data assessment, which leads to incorrect estimation of flow and perfusion rate.^[81,122–124] As far as all biological tissues compose both dynamic and static (e.g., skull, skin, etc.) components, the issue of non-ergodicity is critical for DLS-based techniques. Beside the issues described above, the unknown form of the field correlation functions also limits the DLS’s ability for quantitative measurements.

Limitations are attributed to the features and properties of actual experimental setups/conditions and software for data processing. For example, considering hardware for DLS-based measurements, LDF, for example, requires the implementation of a scanning mode for assessment of blood flow in large areas, resulting in an increase of the measurement time.

As far as LDF-based modalities require either a scanning mode spectrometer or swept laser source, the similar shortcomings of LDF are attributed to DOCT. The results of Doppler measurements are highly sensitive to the angle between the scanning beam and the angle of observation (known as the Doppler angle), which drastically limits the accuracy in clinical practice.^[153] Despite the attempts to achieve angle-independent Doppler measurements, there is still up to 12% uncertainty in the measured velocity values.^[154]

Finally, considering software and data processing, the main disadvantage of commonly used spatial algorithms in DLS-based imaging approaches is the loss of spatial resolution determined by the sliding window size (see above).

3. Recent Progress in DLS-Based Imaging of Blood Flow

3.1. Accuracy Improvement

The advances in DLS-based imaging of blood flow in vivo have expanded its capabilities, improved its resolution and quantification, and broadened its applications in both research and clinical domains. Careful design of experiments and data analysis are required to ensure the validity of Siegert’s relation, particularly in situations where ergodicity is uncertain or violated. In fact, in many practical cases of the application of DLS-based modalities for characterization of blood flow in biological tissues, the assumption of ergodicity cannot be fulfilled due to the complex heterogeneous medium structure. Thus, the relation between $g_2(\tau)$ and $g_1(\tau)$ becomes more complicated or cannot be directly applicable at all.

Recently, to facilitate the fulfillment of ergodicity conditions in blood flow measurements, the parallelized diffuse

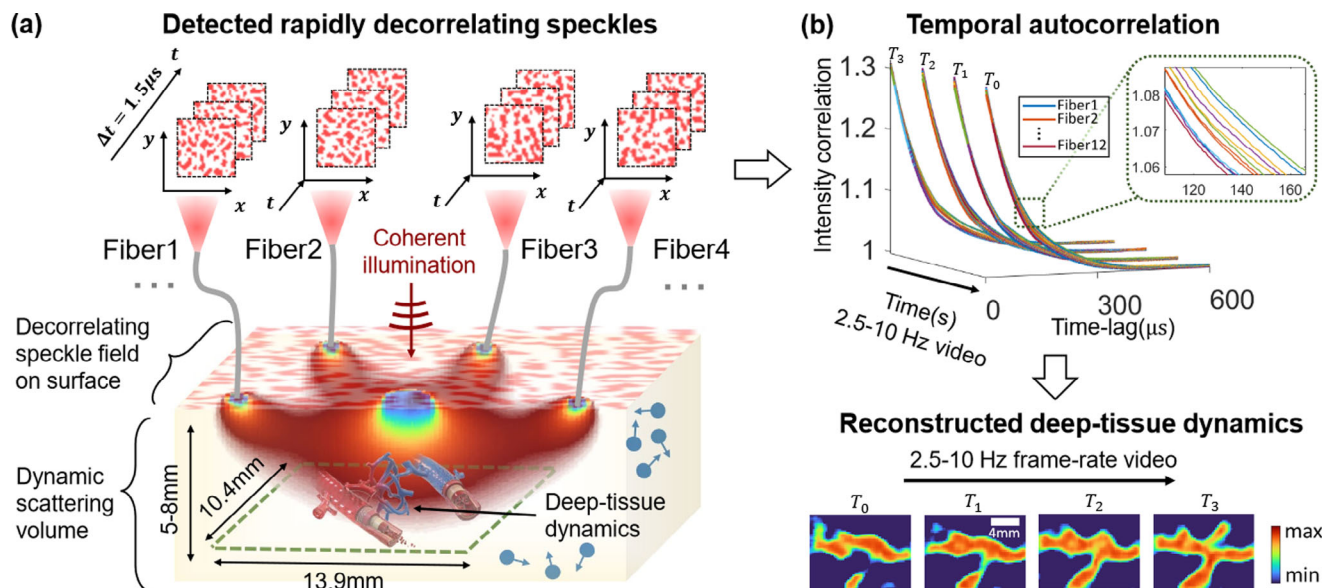


Figure 3. a) Schematic representation of PDCI measurement strategy. Scattered coherent light from a source to multiple detector fibers travels on average through unique banana-shaped paths, dipping $1/2 - 2/3$ of the source-detector separation deep into decorrelating scattering media (e.g., in vivo tissue). Fully developed speckle on the tissue surface rapidly fluctuates as a function of deep-tissue movement. Detected photon paths are assessed by Monte Carlo method and presented for a clear visualization purpose. b) Computed $g_2(\tau)$ curves from time-resolved measurements of surface speckle at different tissue surface locations and corresponding reconstructed dynamic variations occurring beneath the decorrelating scattering material. $g_2(\tau)$ changes are caused by the varying deep-tissue dynamic scattering potentials labeled at the bottom left. Reproduced with permission under terms of the CC BY 4.0 license.^[155] Copyright 2022, The Authors, published by Wiley-VCH GmbH.

correlationimaging (PDCI) approach was introduced.^[155] PDCI provides faster acquisition, wider spatial coverage, improved statistical robustness, and real-time monitoring capabilities. These advantages contribute to a more reliable and comprehensive assessment of blood flow dynamics, supporting the application of PDCI in various research and clinical settings. **Figure 3** illustrates the schematic representation of the signal acquisition principle for PDCI (see **Figure 3a**) and the corresponding reconstructed images showcasing changes in tissue dynamics (see **Figure 3b**).

In fact, the relation between $g_1(\tau)$ and $g_2(\tau)$ depends not only on the coherent properties of light and ergodicity conditions satisfaction, but also on the type of particle motion (ordered or unordered) and regime of light scattering (multiple or single scattering). Postnov et al. generalized the DLS approach by taking into account the parameters of the experiment and the peculiarities of the dynamic medium

$$g_2(\tau) = 1 + \beta \rho^2 (d |g_1^{n=X}(\tau)| + (1-d) |g_1^{n=1}(\tau)|)^2 + \beta^{1/2} (1-\rho) \rho (d |g_1^{n=X}(\tau)| + (1-d) |g_1^{n=1}(\tau)|) + C \quad (16)$$

where $g_1^n(\tau) = \exp(-(\tau/\tau_c)^n)$, C is the offset caused by noise, X and d depends on type of dynamics (multiple scattering from unordered motion, single scattering from ordered motion and single scattering from unordered or multiple scattering from ordered motion).^[156] **Figure 4** shows schematically the DLS/DWS blood flow imaging setup and processing principles (see **Figure 4a**), as well as principles of judgment on types of blood dynamics (see **Figure 4b**).

Du et al. introduced the combined use of surface illumination laser speckle contrast imaging (SI-LSCI) and line scan laser speckle contrast imaging (LS-LSCI) modes, that is allowed for imaging of small vessels at deeper depths compared to common LSCI setup.^[157] Optical speckle image velocimetry (OSIV) technique is developed for quantitative flow estimation.^[158]

Wu et al.^[159] proposed a fitting procedure based on computer simulation, allowing for more precise determination of blood flow index (BFI) values during human cerebral perfusion assessment. A series of works showed the possibility to increase SNR by using multi-source and parallel detection for DWS. The most convenient way to improve SNR is to increase amount of probing light. However, high exposure to laser light can be dangerous for biological tissue. Thus, Dietsche et al.^[133] proposed to use multiple photon counting detection channels to obtain data from multiple speckles. With further developments this approach is improved by the use of single photon avalanche diodes (SPAD) camera.^[160,161] Another way to increase SNR is suggested by Robinson et al.^[162] Particularly, the proposed heterodyne interferometric detection by adding the reference arm to the DWS system is doubling SNR in $g_2(\tau)$ measurements. The proposed approach allows for the use of cheaper cameras for data registration. Several studies introduce a combined use of heterodyne detection and parallel detection using high-speed line scan cameras.^[163-166] These approaches also demonstrated better accuracy and quality of measurements compared to standard DWS, even without the use of the reference arm. A few approaches were proposed to improve the sensitivity of DWS in deep tissue layers. Particularly, acoustic tagging,^[167] time-resolved DWS,^[168] and path length selection via coherence gating^[169] approaches are introduced. These techniques allow to improve resolution by

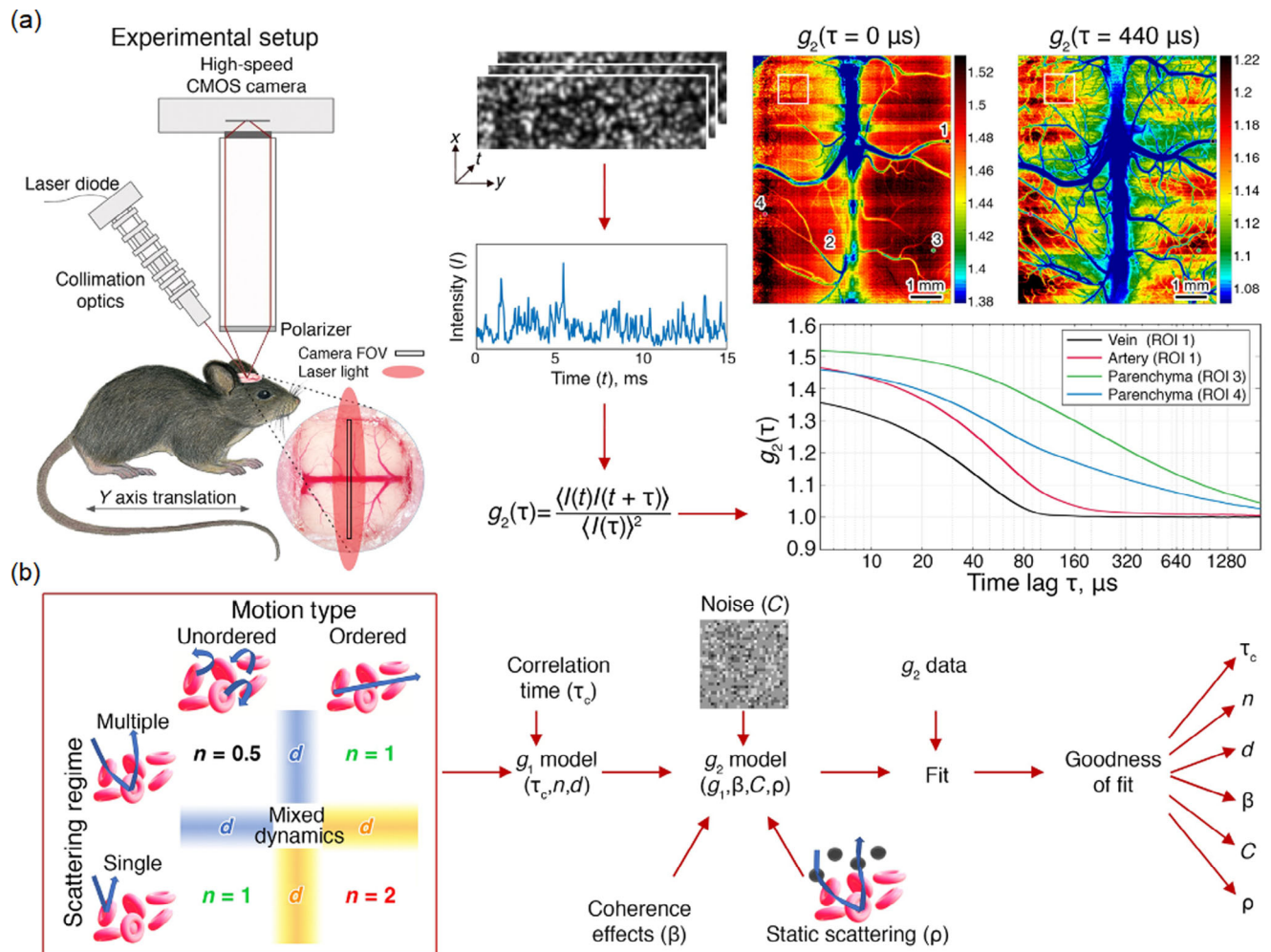


Figure 4. a) Schematic presentation of DLS-based blood flow imaging experimental setup and processing principles, as well as the maps of spatial distribution of blood flow in terms of $g_2(\tau)$ for $\tau = 0$ and $440 \mu\text{s}$ with corresponding quantitative data; b) Principles of the model and fitting process. Reproduced with permission.^[156] Copyright 2020, The Authors; exclusive licensee American Association for the Advancement of Science. No claim to original U.S. Government Works. Distributed under a Creative Commons Attribution License 4.0 (CC BY).

isolating deep tissue probing photons and the photons from superficial layers. It was also demonstrated that the use of longer wavelengths allows increased probing depth in DWS.^[170] With the main aim to optimize and speed up data processing for LSCI, Ansari et al.^[171] implemented an algorithm based on the motion history image method, allowing to identify only the areas where blood flow changed over time. The proposed algorithm was verified by rodent brain vasculature assessment during spreading depolarization and cardiac arrest.

3.2. Brain Vasculature Assessment

As far as DLS-based techniques do not require any contrast agents for blood flow visualization and also provide fast, non-contact, full-field (in the case of LSCI) assessment of microvasculature with high spatial and temporal resolution, this method is widely used for brain vasculature visualization in clinical applications and in animal models. The CBF response to cardiac

arrest and its relation to mean arterial pressure have been investigated in ref. [172]. The continuous monitoring of CBF changes at the level of individual vessels in rodents treated by the target temperature management method after cardiac arrest has been achieved.^[172,173] With the further development of approach, the CBF changes caused by cerebral ischemia re-perfusion injury were monitored.^[174] Besides, different approaches for assessment of CBF changes during activation in the somatosensory cortex by repetitive whisker stimulation have been analyzed.^[175] It has been shown that principal component analysis (PCA) can significantly reduce the noise in speckle contrast data. The fast Fourier transform and general linear model analysis were performed to estimate the cortex activation.

Further, Pavlov et al.^[176] showed that CBF in large and small cerebral blood vessels changes differently under variations in peripheral arterial pressure induced by mesaton injection.

Venugopal et al.^[177] investigated the CBF response to a cistern magna injection, which is widely used to mimic aneurysmal subarachnoid hemorrhage. The speckle pattern fractal analysis based

on the Hurst exponent showed better sensitivity in the assessment of CBF changes during aneurysmal subarachnoid hemorrhage compared to common LSCI analysis. The described approach is also used for subdermal or retinal imaging. Cumsille et al.^[178] demonstrated using the animal model that the brain perfusion calculated by LSCI is different in case of the reduced placental perfusion model of preeclampsia comparing to the respective controls.

Chen et al.^[97] proposed to use standard LSCI in combination with microendoscopy to measure CBF response to hemodynamic changes at the subcortical level of the brain. Uchida et al.^[179] in vivo investigated the release of acetylcholine as well as changes in blood flow in the olfactory bulb in response to focal stimulation of the horizontal limb of the diagonal band of Broca using LSCI and microdialysis. A series of works^[180–182] presents studies of CBF and brain electrophysiology monitoring before, during, and after asphyxial cardiac arrest and further resuscitation using LSCI and LSCI combined with electroencephalography. Zhao et al.^[183] showed the possibility to use nanosecond pulse laser sources in LSCI setups for CBF measurements. The use of pulsed light sources will possibly allow for combined LSCI-photoacoustic imaging. Mangraviti et al.^[184] presented system allowing for real-time projection of speckle contrast images with high spatial and temporal resolution to the eyepiece of the surgical microscope as a direct overlay on the morphological image. Liu et al.^[185] presented short-separation speckle contrast optical spectroscopy utilizing point illumination and point detection by multi-mode fiber arrays. The proposed technique has been verified during post-stroke brain vasculature observation in an animal model and allowed to improve signals from static and slow tissue components compared to standard LSCI.

Piavchenko et al.^[186] reported the application of a multimodal approach combining LSCI, fluorescence spectroscopy, and diffuse reflectance spectroscopy allowing to discriminate post-mortem processes in the mouse brain vasculature after cardiac arrest and respiratory arrest. It was shown that cardiac arrest is more life-threatening compared to respiratory arrest since blood flow in the cerebral cortex vascular network stops 2 min after respiratory arrest while after cardiac arrest the blood flow stops just in 1 min. Also, the authors showed that brain oxygen saturation increased after cardiac arrest, while for respiratory arrest it had almost no changes. **Figure 5** illustrates variations in speckle contrast images depicting brain vasculature following distinct conditions: cardiac arrest (as depicted in Figure 5a) and respiratory arrest (as depicted in Figure 5b).

In order to overcome the described issue and provide a more precise CBF assessment, Kalchenko et al. suggested to adjust speckle contrast values accordingly to distribution time of fluorescent agents in the brain vasculature.^[187] This approach provides more relevant and adequate information on flow rate ratios between different types of vessels.

Figure 6 presents a comprehensive overview of the LSCI-FIM setup, comprising an optical scheme (see Figure 6a), the underlying image processing principles (see Figure 6b), and practical illustrations, including a CCDF image (see Figure 6c), a fluorescence time-to-maximum image (see Figure 6e), and speckle contrast images both before (see Figure 6d) and after (see Figure 6f) the correction procedure. In addition, Figure 6g provides a comparative analysis of speckle contrast values calculated prior to

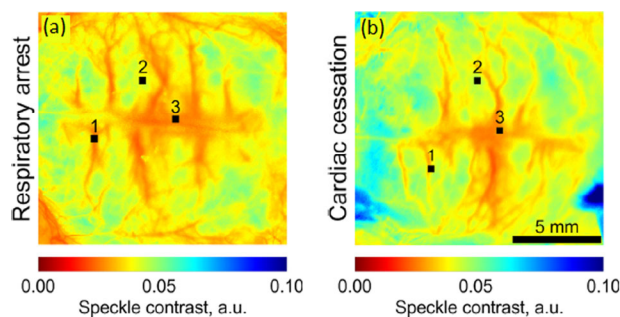


Figure 5. Transcranial LSCI images during a) respiratory arrest and b) cardiac cessation, showing: veins of medium caliber (1), vessels of microcirculation (2), and venous sinus (3). Reproduced with permission under terms of the CC-BY 4.0 license.^[186] Copyright 2021, The Authors, published by Wiley-VCH GmbH.

and following the correction process, offering valuable insights into the effectiveness of the correction. Early on, a combined use of LSCI and FIM was implemented for monitoring blood and lymph microflows in tumors,^[151,188,189] as well as for visualization of the skin vascular network^[41,190] and tumor surroundings.^[191]

The above described results of LSCI application for brain CBF assessment have been implemented using animal models. In fact, further studies present the use of LSCI for human cortical blood flow imaging during neurosurgical procedures.

Richards et al. implemented multi-exposure speckle imaging combined with neurosurgical microscope CBF imaging with higher sensitivity.^[192] Miller et al. used LSCI for CBF assessment during cerebral aneurysm surgery and arteriovenous malformation resection in humans.^[193] Tao et al. applied LSCI for CBF control during arteriovenous malformation resection,^[194] demonstrating that LSCI is highly effective for real-time detection of pathological hyperperfusion at decent spatial-temporal resolution. Guo et al. proposed random matrix-based LSCI for intraoperative laparoscopic surgery.^[195] This approach was validated on the rat and swine model. Ideguchi et al. demonstrated that LSCI use during neurosurgery allows for real-time recognition of mass lesion-related vasculature, which may be used to avoid ischemic complications.^[196] In addition to direct measurement of CBF, Kalyuzhner et al. presented an approach for remote monitoring and detection of human cortex responses to different senses (hearing, taste, and smell).^[197] The proposed approach is based on the assessment of nano-vibrations generated by the blood flow in specific regions of the brain using spatio-temporal analysis of self-interference random speckle patterns. Kim et al.^[198] implemented speckle contrast optical spectroscopy at large source-detector separations, which improved sensitivity to CBF changes rather than extracerebral blood flow changes in the human brain.

3.3. Skin Perfusion Monitoring

Observation of blood flow in a single vessel is complicated for the skin due to the fact that the skin vasculature is located mostly in the dermis. Moreover, a high scattering of epidermis limits the probing depth of DLS-based techniques and introduces the effects of non-ergodicity. Nonetheless, it was found that LSCI and

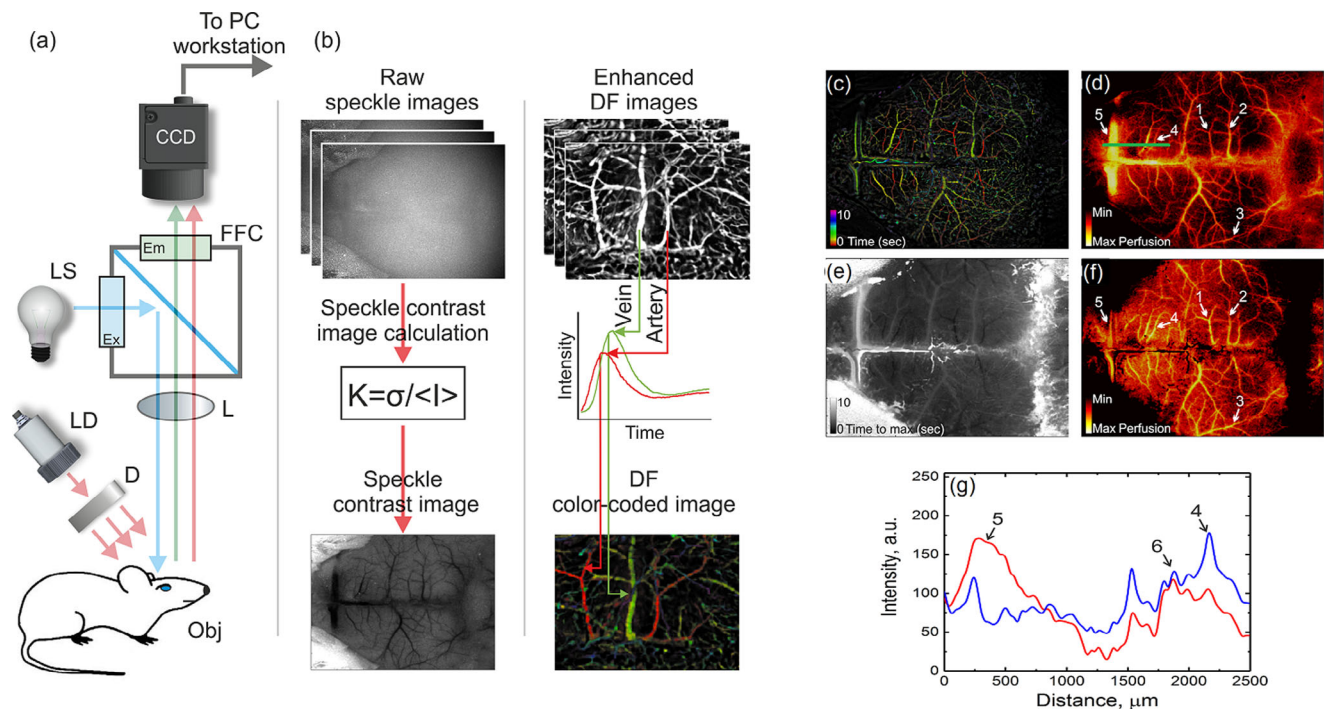


Figure 6. a) Schematic presentation of principles of operation of the combined laser speckle contrast imaging and fluorescent intravital microscopy (LSCI-FIM) experimental system. CCD represents the CCD camera, LS is the light source for fluorescence imaging, Ex is the excitation optical filter, Em is the emission band-pass filter, FFC is the fluorescence filter cube, L is the lens, D is the diffuser, LD is the laser diode for speckle imaging, and Obj is the object of investigation. b) Principles of speckle contrast image calculation and color-coded dynamic fluorescent (CCDF) images calculation. c) CCDF image of a mouse brain distinguishing veins and arteries. Red colors correspond to arteries, whereas green colors correspond to veins. d) Speckle contrast image of mouse brain before correction procedure. e) Fluorescence time to maximum image. f) Speckle contrast image of mouse brain after correction procedure. Scale bar (white line) is equal to 1 mm. The green line represents the line for contrast intensity profile calculation. g) Contrast intensity profiles of lines (marked by green in (d) and (f)) across the speckle contrast images before and after the correction procedure. The red line corresponds to the contrast intensity profile of the speckle contrast image before the correction procedure. The blue line corresponds to the contrast intensity profile of the speckle contrast image after the correction procedure. Points 4, 5, and 6 correspond to the artery, sagittal sinus, and vein (same points in (d) and (f)). Reproduced with permission under terms of the CC-BY 4.0 license.^[187] Copyright 2019, The Authors, Licensee MDPI, Basel, Switzerland.

LDF approaches allow for the observation of skin blood perfusion changes. Particularly, LSCI is extensively used for assessment of wounds, burns, and ulcers healing monitoring, port wine stain (PWS) birthmark treatment, perfusion studying, and so on.^[187,199–205]

Güven et al.^[206] presented a comparison of LSCI with LDF perfusion imaging for tissue perfusion assessment. Both techniques showed a strong linear correlation in perfusion measurements. Li et al.^[207] demonstrated a transmissive-detected laser speckle contrast imaging (TR-LSCI) approach allowing to visualize vessels deeply located in tissue. **Figure 7** provides a comprehensive comparison between conventional LSCI and TR-LSCI approaches.

Mirdell et al. demonstrated that LSCI can be effectively used as a supportive tool for monitoring and assessment of burn healing process,^[208] assessment of scald wound healing^[200,209] and prediction of psoriasis lesions expansion.^[210,211]

LSCI allows prediction accurately surgical need in scald burns, especially in a short period after injury study.^[209] Compared to conventional LDF imaging, LSCI is faster and less sensitive to motion artifacts technique. Being successfully implemented for the assessment of the depth of the scald wound.^[200] LSCI has

the potential to improve the evaluation of healing procedures and decrease the duration of burn care.

Considering LDF measurements, the decomposition of LDF power spectra in terms of ranging blood flow distribution by frequency series allowed to significantly improve the accuracy for blood flow measurements.^[144] **Figure 8** shows a photo of the combined optical probe and heating element located at the volunteer's foot (Figure 8a), study protocol (Figure 8b) and an example of calculated blood perfusion changes (Figure 8c).

Couturier et al. implemented combined LSCI, LDF, and reflectance oximetry for monitoring skin perfusion during wound healing.^[212] It has been demonstrated, that LSCI provides good repeatability in determining between healthy and wounded skin area.

Systemic sclerosis (SSc) is rare connective tissue disease that can be characterized by microvascular system alterations and decreased peripheral blood perfusion resulted in tissue fibrosis and increased chance of digital ulcers (DU) formation.^[213] Ruaro et al. pioneered the use of LSCI for evaluation of both local blood perfusion and DU area evolution during SSc treatment,^[214] and explored correlation between blood perfusion and dermal thickness in different skin areas of SSc patients.^[215]

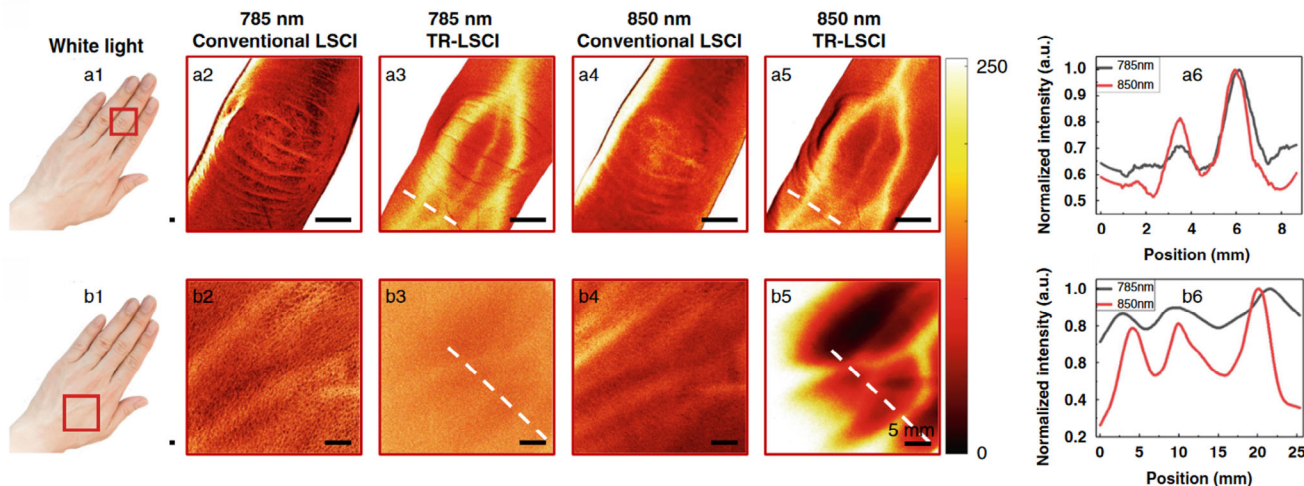


Figure 7. Comparison of conventional LSCI and TR-LSCI for blood flow mapping in human hand. Reproduced with permission under terms of the CC-BY 4.0 license.^[207] Copyright 2021, The Authors, published by Springer Nature.

Barsotti et al. confirmed the importance of LSCI application for monitoring DU evolution.^[201]

Among the DU monitoring methods, LSCI is also widely used for assessment of microcirculation in diabetic foot ulcers.^[216,217]

LSCI has been implemented for monitoring blood perfusion in human eyelid skin flaps.^[202] It was shown that blood perfusion rapidly decreases with the distance from the base of the skin flaps on the eyelid. Additionally, the use of LSCI allowed to estimate optimal width and length of skin flaps for plastic surgery. Further, the same research group presented results on investiga-

tion of perfusion in human upper eyelid flaps under different degrees of flap stretching and rotation.^[218] LSCI has been used for re-perfusion monitoring during skin grafting^[219] and glabellar flap,^[220] for re-vascularization monitoring after H-plasty reconstructive surgery,^[221] perfusion mapping during full-thickness blepharotomy,^[222] and eye muscle surgery.^[223] The combined hyperspectral imaging and LSCI approach has been used for perfusion assessment after anesthetic injection during oculoplastic surgery.^[224,225]

Chen et al. showed that keloids can have different stages during their growth and treatment.^[226] Particularly, keloids in the progressive stage can be characterized by a high perfusion rate compared to stable and regressive stages. Recently, Li et al. demonstrated combined use of LSCI and deep learning algorithms for evaluation of keloids states.^[227] Data from 150 patients in total were analyzed and proposed approach showed high accuracy in keloids classification.

3.4. DLS in Tissues with Controlled Optical Parameters

Last decade, optical clearing became an effective technique for improvement of probing depth and data quality during biomedical optical imaging.^[228] The studies have revealed that applying an optical clearing agent to the mouse skull, with subsequent skin removal, enables visualization of brain vasculature.^[229] This involves applying a mixture of dimethylsulfoxide, aurinol, weak alkaline substances, alcohol, EDTA, sorbitol, and glucose to the skull for 25 min. Zhang et al.^[230] developed switchable optical clearing method.

The proposed method permits vascular development observation using LSCI for both short-term (daily for a week) and long-term (monthly for six months) periods. It involves skin removal and is applicable to mice aged 2–8 months with relatively thin skulls. Kalchenko et al. showed that 20 min application of a mixture (50/50) of liquid paraffin oil and glycerol to mouse skin allowed for fully non-invasive in vivo brain

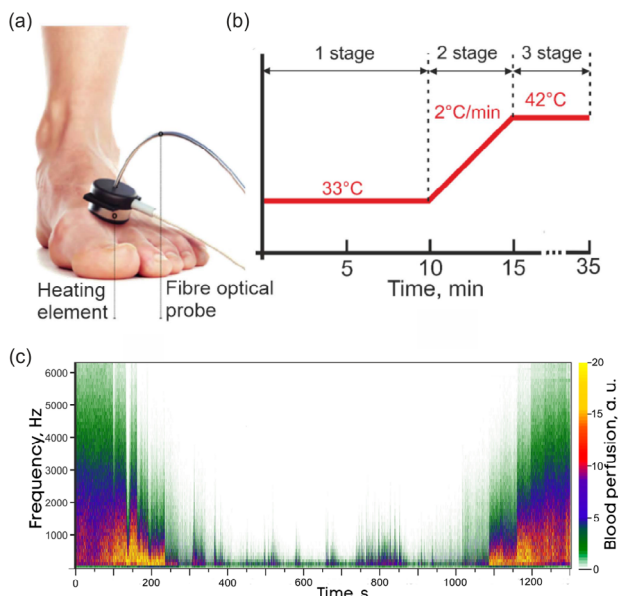


Figure 8. a) Demonstration the fibre optical probe location on the volunteer's foot. b) Study protocol with the heat test. c) A relevant example of the distribution of calculated blood perfusion by frequency of Doppler shift for local pressure. Reproduced with permission under the terms of the CC-BY license.^[144] Copyright 2022, The Authors, published by IEEE.

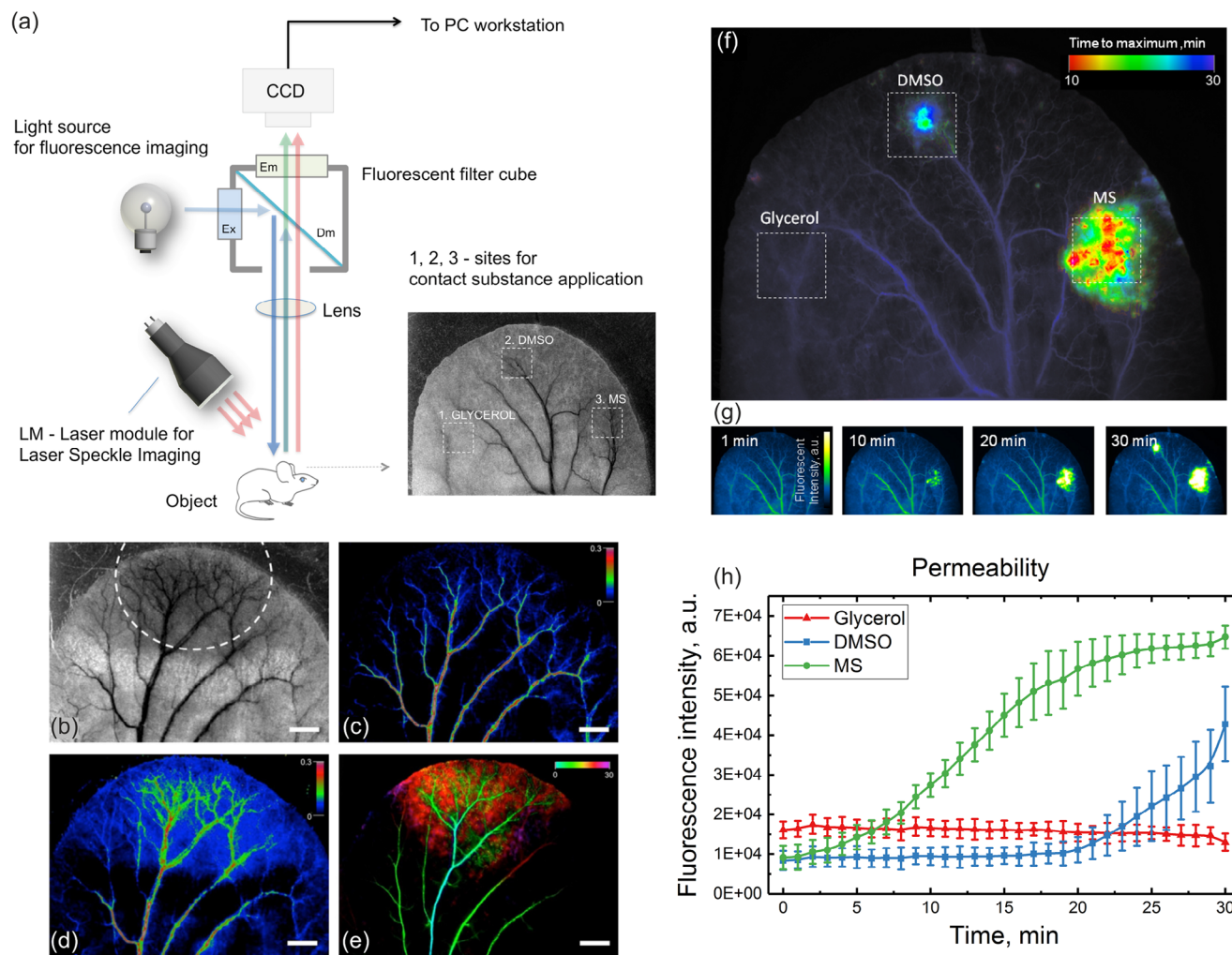


Figure 9. a) LSCI-FIM imaging system. The areas of topical application of glycerol, DMSO, and MS are marked by white squares. b) The monochrome image of the area of methyl salicylate (MS) agent topical application (highlighted by the dashed line), obtained by LSCI mode with the long (650 ms) exposure time. (c,d) show, respectively, the color-coded images before and after 30 min of MS agent application. e) Temporal color-coded image of the same area of mouse ear observed in the FIM mode after injection of FITC-Dextran. White bar is 1 mm. f) Fluorescent pseudocolor images of the external mouse ear in vivo. Squared dashed line highlights the places of the contact glycerol, DMSO, and MS applications: Color-coded bar represents time to maximum intensity (in minutes). g) Sequence of fluorescent pseudocolor images of the same external mouse ear in vivo at a different time points after the chemical agent application. h) Evolution of fluorescence intensity during the application of selected contact substances to the external mouse ear in vivo. Reproduced with permission under the terms of the CC-BY license.^[188] Copyright 2019, The Authors, published by SPIE under a Creative Commons Attribution 4.0 Unported License.

vasculature assessment.^[231] The acute vascular permeability response of mouse skin to various clearing agents, including glycerol, DMSO, and methyl salicylate (MS), was comprehensively investigated using LSCI-FIM.^[232]

The basics of the LSCI-FIM setup are presented in **Figure 9**. It includes (see **Figure 9b,c**) illustrative monochrome images displaying speckle contrast as well as FIM color-coded images (see **Figure 9d,e**) of a mouse ear captured while applying only microspheres (MS). Additionally, it showcases fluorescent images of the mouse ear obtained following the application of microspheres (MS), glycerol, and DMSO (see **Figure 9f,g**). Furthermore, **Figure 9h** provides quantitative data, presenting changes in fluorescence intensity resulting from the application of these agents.

3.5. Future Perspectives

The tissue movement artifacts are the critical issues limiting the clinical application of LSCI. As far as any movements of an observed object result in changes in the measured speckle contrast value, the development of the motion artifact correction approaches is an important goal for speckle contrast imaging. Several articles presented methods for motion artifact correction in LSCI, including software^[172,233] and hardware^[234,235] solutions. Based on a time-space Fourier transformation Molodij et al. suggested a technique for motion artifacts correction using the LSCI-FIM setup.^[145] **Figure 10** shows the principle of time-space Fourier filtering and corresponding brain vasculature images after filtering with different criteria.

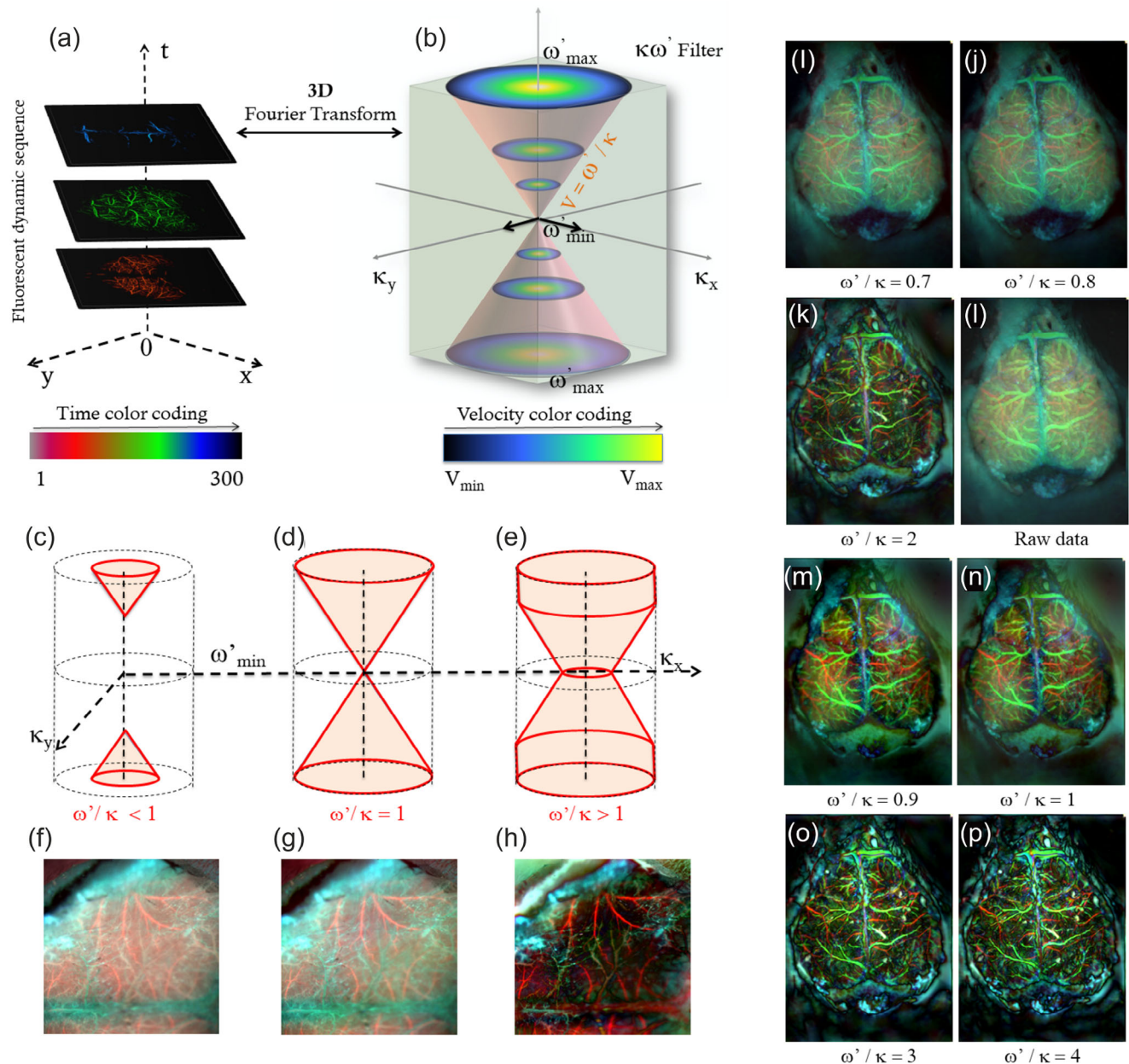


Figure 10. a) Temporal color coding procedure applied along the frame sequence to distinguish the time-evolution structures in brain. b) The principle of time-space Fourier filtering. c–e) Examples of the removed volume in the Fourier frequencies indicated in pink. f–h) Time color-coded images after the $\kappa\omega'$ filtering for different velocity criterion $v = \omega'/\kappa$. i–p) Comparison of the filtering efficiency on the same temporal sequence for different velocity criterion. Reproduced with permission under the terms of the CC-BY license.^[145] Copyright 2020, The Authors, published by the Institute of Physics and Engineering in Medicine.

Development of multi-modal approaches combining DLS with other imaging and electrophysiological modalities, such as OCT, FIM, etc. has great potential for clinical implementation since it allows for multi-parameter monitoring of biological processes. Arguably, further development of DLS-based approach will be associated with the implementation of artificial intelligence (AI), machine learning and deep-learning algorithms,^[236] and embedding shaped light carrying orbital angular momentum (OAM).^[237] The implementation of OAM to the DLS-based imaging approach holds several intriguing perspectives. i) Enhanced

spatial resolution: The laser beams possessing OAM originate smaller speckles due to scattering, enabling the detection of finer flow details and better resolution of blood dynamics in smaller vessels or localized regions. ii) Probing depth discrimination: By incorporating OAM light with different helical states or orbital numbers, it becomes possible to selectively probe blood flow at distinct depths within the tissue. This could enable the assessment of blood flow dynamics in different layers of the microvasculature. iii) Flow direction awareness: By designing OAM modes with different helical charges, the direction of blood flow

can be tracked. Indeed, while the integration of OAM into DLS imaging of blood flow holds significant potential, it is important to note that this is still an emerging area of research. But continued research and technological advancements in DLS-based imaging approaches will pave the way for exciting developments and new insights into blood flow diagnostic imaging in the future.

4. Conclusions

In the current paper, we review the foundational principles, recent developments, as well as newly emerging implementations and advancements in DLS imaging of blood flow and blood microcirculations. While certain limitations remain, such as challenges in establishing a precise quantitative correlation between measured data and actual physiological parameters, limited probing depth, and considerations related to ergodicity, it is noteworthy that DLS-based methodologies, specifically DWS, LSCI, and LDF, have exhibited notable success in various practical biomedical applications. These applications include, but are not limited to, full-field transcranial brain blood flow imaging in live subjects, skin perfusion measurements, non-invasive blood microcirculation imaging, and functional imaging.

Remarkable advancements in technology and image processing have empowered researchers to enhance DLS-based techniques significantly. These enhancements encompass improvements in spatial and temporal resolution, as well as the quality of measured data, thereby augmenting precision and accuracy. Notably, the cost-effectiveness of essential instrumentation, the ease of implementation, and the affordability of optical components utilized in measurements underscore the invaluable resource that the DLS-based approach has become for clinical applications.^[238]

Furthermore, the integration of DLS with other imaging and electrophysiological modalities holds great promise for multi-parameter recording of intricate biological phenomena. This multi-modal approach stands poised to provide a deeper understanding of complex physiological processes.

In summary, the evolution of DLS in the context of blood flow and blood microcirculation imaging has expanded its capabilities, refined its resolution and quantification, and broadened its scope across both research and clinical domains. The continued exploration of DLS in biomedical imaging is expected to yield further breakthroughs, advancing our understanding of dynamic physiological processes and enhancing healthcare applications.

Acknowledgements

All authors contributed equally to this work. Authors acknowledge the support provided by the Russian Science Foundation (project no. 22-65-00096) and European Union's Horizon 2020 Research and Innovation Programme under grant agreement No. 863214 – NEUROPA project.

Conflict of Interest

The authors declare no conflict of interest.

Keywords

blood flow, diffusing wave spectroscopy, Doppler optical coherence tomography, dynamic light scattering, laser Doppler flowmetry, laser speckle contrast imaging, microcirculation

Received: May 30, 2023

Revised: October 12, 2023

Published online:

- [1] B. Crosignani, *Statistical Properties of Scattered Light*, Elsevier, London **1975**.
- [2] H. Cummins, *Photon Correlation Spectroscopy and Velocimetry*, Vol. 23, Springer Science & Business Media, Berlin **2013**.
- [3] A. P. Shepherd, P. Å. Öberg, *Laser-Doppler Blood Flowmetry*, Vol. 107, Springer Science & Business Media, Berlin **2013**.
- [4] B. J. Berne, R. Pecora, *Dynamic Light Scattering: With Applications to Chemistry, Biology, and Physics*, Courier Corporation, North Chelmsford **2000**.
- [5] M. Giglio, in *Lasers in Biology and Medicine* (Eds: F. Hillenkamp, R. Pratesi, C. A. Sacchi), Springer, Boston, MA **1980**, pp. 111–126.
- [6] H. Z. Cummins, E. R. Pike, *Photon Correlation and Light-Beating Spectroscopy*, NATO Advanced Study Institute Series, Vol. 3, Springer, Boston, MA **1974**.
- [7] R. Pecora, *Dynamic Light Scattering: Applications of Photon Correlation Spectroscopy*, Springer Science & Business Media, Berlin **2013**.
- [8] H. Z. Cummins, H. L. Swinney, in *Progress in Optics*, Vol. 8, Elsevier, London **1970**, pp. 133–200.
- [9] A. T. Forrester, R. A. Gudmundsen, P. O. Johnson, *Phys. Rev.* **1955**, 99, 1691.
- [10] R. H. Brown, R. Q. Twiss, *Nature* **1956**, 177, 27.
- [11] H. Cummins, N. Knable, Y. Yeh, *Phys. Rev. Lett.* **1964**, 12, 150.
- [12] C. Riva, B. Ross, G. B. Benedek, *Invest. Ophthalmol. Visual Sci.* **1972**, 11, 936.
- [13] M. Stern, *Nature* **1975**, 254, 56.
- [14] M. Stern, D. Lappe, P. Bowen, G. Chimosky, G. Holloway Jr, H. Keiser, R. Bowman, *Am. J. Physiol.* **1977**, 232, H441.
- [15] G. A. Holloway Jr, D. W. Watkins, *J. Invest. Dermatol.* **1977**, 69, 3.
- [16] R. Bonner, R. Nossal, *Appl. Opt.* **1981**, 20, 2097.
- [17] P. A. Öberg, *Crit. Rev. Biomed. Eng.* **1990**, 18, 125.
- [18] R. J. Gush, T. A. King, M. I. V. Jayson, *Phys. Med. Biol.* **1984**, 29, 1463.
- [19] G. Maret, P. Wolf, *Z. Phys. B: Condens. Matter* **1987**, 65, 409.
- [20] D. Pine, D. Weitz, P. Chaikin, E. Herbolzheimer, *Phys. Rev. Lett.* **1988**, 60, 1134.
- [21] D. J. Pine, D. A. Weitz, J. X. Zhu, E. Herbolzheimer, *J. Phys.* **1990**, 51, 2101.
- [22] P. D. Kaplan, M. H. Kao, A. G. Yodh, D. J. Pine, *Appl. Opt.* **1993**, 32, 3828.
- [23] D. A. Weitz, J. X. Zhu, D. J. Durian, H. Gang, D. J. Pine, *Phys. Scr.* **1993**, 1993, 610.
- [24] D. A. Boas, L. E. Campbell, A. G. Yodh, *Phys. Rev. Lett.* **1995**, 75, 1855.
- [25] S. E. Skipetrov, I. Meglinski, *J. Exp. Theor. Phys.* **1998**, 86, 661.
- [26] I. Meglinski, D. A. Boas, A. G. Yodh, B. Chance, V. V. Tuchin, *Izv. VUZ. Appl. Nonlinear Dyn.* **1996**, 4, 72.
- [27] I. Meglinski, D. A. Boas, A. G. Yodh, B. Chance, in *Nonlinear Dynamics and Structures in Biology and Medicine: Optical and Laser Technologies: International Workshop* (Ed: V. V. Tuchin), Vol. 3053, SPIE, Bellingham, WA **1997**, pp. 34–41.
- [28] D. A. Boas, A. G. Yodh, *J. Opt. Soc. Am. A* **1997**, 14, 192.
- [29] A. N. Korolevich, I. Meglinski, *Bioelectrochemistry* **2000**, 52, 223.

- [30] C. Cheung, J. P. Culver, K. Takahashi, J. H. Greenberg, A. G. Yodh, *Phys. Med. Biol.* **2001**, *46*, 2053.
- [31] J. Li, G. Dietsche, D. Iftime, S. E. Skipetrov, G. Maret, T. Elbert, B. Rockstroh, T. Gisler, *J. Biomed. Opt.* **2005**, *10*, 44002.
- [32] G. Yu, T. Durduran, C. Zhou, H. W. Wang, M. E. Putt, H. M. Saunders, C. M. Sehgal, E. Glatstein, A. G. Yodh, T. M. Busch, *Clin. Cancer Res.* **2005**, *11*, 3543.
- [33] G. Dietsche, M. Ninck, C. Ortolof, J. Li, F. Jaillon, T. Gisler, *Appl. Opt.* **2007**, *46*, 8506.
- [34] I. Meglinski, V. V. Tuchin, *Diffusing Wave Spectroscopy: Application for Blood Diagnostics*, Springer, New York **2013**.
- [35] M. Ninck, M. Untenberger, T. Gisler, *Biomed. Opt. Express* **2010**, *1*, 1502.
- [36] Z. Hajjarian, S. Nadkarni, *Sci. Rep.* **2012**, *2*, 316.
- [37] T. Durduran, A. G. Yodh, *NeuroImage* **2014**, *85*, 51.
- [38] S. A. Carp, M. B. Robinson, M. A. Franceschini, *Neurophotonics* **2023**, *10*, 013509.
- [39] A. Fercher, J. Briers, *Opt. Commun.* **1981**, *37*, 326.
- [40] R. Bandyopadhyay, A. Gittings, S. Suh, P. Dixon, D. Durian, *Rev. Sci. Instruments* **2005**, *76*, 093110.
- [41] V. Kalchenko, N. Madar-Balakirski, I. Meglinski, A. Harmelin, *J. Biophotonics* **2011**, *4*, 645.
- [42] J. D. Briers, S. Webster, *J. Biomed. Opt.* **1996**, *1*, 174.
- [43] A. K. Dunn, *Ann. Biomed. Eng.* **2012**, *40*, 367.
- [44] Y. Tamaki, M. Araie, E. Kawamoto, S. Eguchi, H. Fujii, *Invest. Ophthalmol. Visual Sci.* **1994**, *35*, 3825.
- [45] M. Roustit, C. Millet, S. Blaise, B. Dufournet, J. L. Cracowski, *Microvasc. Res.* **2010**, *80*, 505.
- [46] N. Hecht, J. Woitzik, J. P. Dreier, P. Vajkoczy, *Neurosurg. Focus* **2009**, *27*, E11.
- [47] A. Khalil, A. Humeau-Heurtier, G. Mahé, P. Abraham, *J. Biomed. Opt.* **2014**, *20*, 51010.
- [48] A. M. Hamed, H. El-Ghandour, F. El-Diasty, M. Saady, *Opt. Laser Technol.* **2004**, *36*, 249.
- [49] T. Yoshimura, K. Kato, K. Nakagawa, *J. Opt. Soc. Am. A* **1990**, *7*, 2254.
- [50] Y. Kuznetsov, A. Sdobnov, I. Meglinski, A. Harmelin, V. Kalchenko, *Laser Phys. Lett.* **2019**, *16*, 115601.
- [51] R. Arizaga, E. E. Grumel, N. Cap, M. Trivi, J. I. Amalvy, B. Yepes, G. Ricaurte, *J. Coat. Technol. Res.* **2006**, *3*, 295.
- [52] D. Huang, E. A. Swanson, C. P. Lin, J. S. Schuman, W. G. Stinson, W. Chang, M. R. Hee, T. Flotte, K. Gregory, C. A. Puliafito, J. G. Fujimoto, *Science* **1991**, *254*, 1178.
- [53] V. Westphal, S. Yazdanfar, A. M. Rollins, J. A. Izatt, *Opt. Lett.* **2002**, *27*, 34.
- [54] M. Bonesi, S. Matcher, I. Meglinski, *Laser Phys.* **2010**, *20*, 1491.
- [55] M. Bonesi, D. Y. Churmakov, I. Meglinski, *Meas. Sci. Technol.* **2007**, *18*, 3279.
- [56] M. Bonesi, D. Y. Churmakov, L. J. Ritchie, I. Meglinski, *Laser Phys. Lett.* **2007**, *4*, 304.
- [57] M. Bonesi, S. Proskurin, I. Meglinski, *Laser Phys.* **2010**, *20*, 891.
- [58] V. J. Srinivasan, S. Sakadžić, I. Gorczyńska, S. Ruvinskaya, W. Wu, J. G. Fujimoto, D. A. Boas, *Opt. Express* **2010**, *18*, 2477.
- [59] R. A. Leitgeb, R. M. Werkmeister, C. Blatter, L. Schmetterer, *Prog. Retinal Eye Res.* **2014**, *41*, 26.
- [60] Y. Wang, B. A. Bower, J. A. Izatt, O. Tan, D. Huang, *J. Biomed. Opt.* **2007**, *12*, 041215.
- [61] J. Lee, W. Wu, J. Y. Jiang, B. Zhu, D. A. Boas, *Opt. Express* **2012**, *20*, 22262.
- [62] J. Lee, W. Wu, F. Lesage, D. A. Boas, *J. Cereb. Blood Flow Metab.* **2013**, *33*, 1707.
- [63] C. Papadacci, V. Finel, O. Villemain, G. Goudot, J. Provost, E. Messas, M. Tanter, M. Pernot, *Phys. Med. Biol.* **2019**, *64*, 085013.
- [64] T. Pereira, N. Tran, K. Gadhouri, M. M. Pelter, D. H. Do, R. J. Lee, R. Colorado, K. Meisel, X. Hu, *npj Digital Med.* **2020**, *3*, 3.
- [65] S. Ranjit, L. Lanzano, A. E. Libby, E. Gratton, M. Levi, *Nat. Rev. Nephrol.* **2021**, *17*, 128.
- [66] Y. W. Choo, J. Jeong, K. Jung, *BMB Rep.* **2020**, *53*, 357.
- [67] M. Forcione, A. M. Chiarelli, D. J. Davies, D. Perpetuini, P. Sawosz, A. Merla, A. Belli, *J. Cereb. Blood Flow Metab.* **2020**, *40*, 1586.
- [68] A. B. E. Attia, G. Balasundaram, M. Moothanchery, U. Dinish, R. Bi, V. Ntziachristos, M. Olivo, *Photoacoustics* **2019**, *16*, 100144.
- [69] A. Neprokin, C. Broadway, T. Myllylä, A. Bykov, I. Meglinski, *Life* **2022**, *12*, 588.
- [70] P. Hamelmann, R. Vullings, A. F. Kolen, J. W. Bergmans, J. O. van Laar, P. Tortoli, M. Mischi, *IEEE Trans. Ultrason. Ferroelectr. Freq. Control* **2019**, *67*, 226.
- [71] M. D. Wheelock, J. P. Culver, A. T. Eggebrecht, *Rev. Sci. Instrum.* **2019**, *90*, 051101.
- [72] J. Jonkman, C. M. Brown, G. D. Wright, K. I. Anderson, A. J. North, *Nat. Protoc.* **2020**, *15*, 1585.
- [73] J. Li, X. Wu, Y. Fu, H. Nie, Z. Tang, *Rev. Neurosci.* **2023**, *34*, 559.
- [74] A. Devor, S. Sakadžić, V. J. Srinivasan, M. A. Yaseen, K. Nizar, P. A. Saisan, P. Tian, A. M. Dale, S. A. Vinogradov, M. A. Franceschini, D. A. Boas, *J. Cereb. Blood Flow Metab.* **2012**, *32*, 1259.
- [75] G. Yu, T. Durduran, C. Zhou, R. Cheng, A. G. Yodh, in *Handbook of Biomedical Optics*, CRC Press, Boca Raton, FL **2011**, pp. 195–216.
- [76] R. Bandyopadhyay, A. S. Gittings, S. S. Suh, P. K. Dixon, D. J. Durian, *Rev. Sci. Instrum.* **2005**, *76*, 93110.
- [77] K. Schätzel, *Appl. Phys. B* **1987**, *42*, 193.
- [78] E. Overbeck, C. Sinn, *J. Mod. Opt.* **1999**, *46*, 303.
- [79] E. Jakeman, C. J. Oliver, E. R. Pike, *J. Phys. A: Gen. Phys.* **1970**, *3*, L45.
- [80] D. D. Duncan, S. J. Kirkpatrick, *J. Opt. Soc. Am. A* **2008**, *25*, 2088.
- [81] A. B. Parthasarathy, W. J. Tom, A. Gopal, X. Zhang, A. K. Dunn, *Opt. Express* **2008**, *16*, 1975.
- [82] Y. Deng, D. Chu, *Sci. Rep.* **2017**, *7*, 5893.
- [83] R. Dändliker, F. M. Mottier, *Z. Angew. Math. Phys.* **1971**, *22*, 369.
- [84] A. Einstein, *Ann. Phys.* **1906**, *324*, 371.
- [85] D. A. Boas, I. Meglinski, L. Zeman, L. E. Campbell, B. Chance, A. G. Yodh, in *CIS Selected Papers: Coherence-Domain Methods in Biomedical Optics* (Ed: V. V. Tuchin), Vol. 2732, SPIE, Bellingham, WA **1996**, pp. 34–46.
- [86] M. Heckmeier, S. E. Skipetrov, G. Maret, R. Maynard, *J. Opt. Soc. Am. A* **1997**, *14*, 185.
- [87] D. Bicout, R. Maynard, *Phys. A* **1993**, *199*, 387.
- [88] D. Bicout, G. Maret, *Phys. A* **1994**, *210*, 87.
- [89] T. G. Mason, H. Gang, D. A. Weitz, *J. Opt. Soc. Am. A* **1997**, *14*, 139.
- [90] P. Zakharov, F. Scheffold, in *Advances in Dynamic Light Scattering Techniques*, Springer, Berlin, Heidelberg **2009**, pp. 433–467.
- [91] G. Nisato, P. Hébraud, J.-P. Munch, S. J. Candau, *Phys. Rev. E* **2000**, *61*, 2879.
- [92] F. Scheffold, S. E. Skipetrov, S. Romer, P. Schurtenberger, *Phys. Rev. E* **2001**, *63*, 061404.
- [93] I. Meglinsky, D. Boas, A. Yodh, B. Chance, *Biomedical Optical Spectroscopy and Diagnostics* (Eds: E. Sevcik-Muraca, D. Benaron), Vol. 3, Optica Publishing Group, Washington, D.C **1996**, pp. CM2.
- [94] J. W. Goodman, in *Laser Speckle and Related Phenomena*, Springer, New York **1975**, pp. 9–75.
- [95] J. D. Briers, A. F. Fercher, *Invest. Ophthalmol. Vis. Sci.* **1982**, *22*, 255.
- [96] P. N. Pusey, W. Van Megen, *Phys. A* **1989**, *157*, 705.
- [97] M. Chen, D. Wen, S. Huang, S. Gui, Z. Zhang, J. Lu, P. Li, *Opt. Lett.* **2018**, *43*, 5627.
- [98] Y. Li, R. Liu, Y. Wang, D. Wen, L. Meng, J. Lu, P. Li, *Opt. Express* **2016**, *24*, 8382.
- [99] H. Cheng, T. Q. Duong, *Opt. Lett.* **2007**, *32*, 2188.
- [100] J. Senarathna, A. Rege, N. Li, N. V. Thakor, *IEEE Rev. Biomed. Eng.* **2013**, *6*, 99.
- [101] S. M. S. Kazmi, E. Faraji, M. A. Davis, Y.-Y. Huang, X. J. Zhang, A. K. Dunn, *Biomed. Opt. Express* **2015**, *6*, 2588.

- [102] D. A. Boas, A. K. Dunn, *J. Biomed. Opt.* **2010**, *15*, 11109.
- [103] J. Ramirez-San-Juan, E. Mendez-Aguilar, N. Salazar-Hermenegildo, A. Fuentes-Garcia, R. Ramos-Garcia, B. Choi, *Biomed. Opt. Express* **2013**, *4*, 1883.
- [104] M. A. Davis, L. Gagnon, D. A. Boas, A. K. Dunn, *Biomed. Opt. Express* **2016**, *7*, 759.
- [105] K. Murali, A. Nandakumaran, T. Durduran, H. M. Varma, *Biomed. Opt. Express* **2019**, *10*, 5395.
- [106] D. Briers, D. D. Duncan, E. R. Hirst, S. J. Kirkpatrick, M. Larsson, W. Steenbergen, T. Strömberg, O. B. Thompson, *J. Biomed. Opt.* **2013**, *18*, 66018.
- [107] A. Humeau-Heurtier, P. Abraham, G. Mahe, *IEEE Trans. Med. Imaging* **2013**, *32*, 2311.
- [108] A. K. Dunn, H. Bolay, M. A. Moskowitz, D. A. Boas, *J. Cereb. Blood Flow Metab.* **2001**, *21*, 195.
- [109] H. Cheng, Q. Luo, S. Zeng, S. Chen, J. Cen, H. Gong, *J. Biomed. Opt.* **2003**, *8*, 559.
- [110] S. J. Kirkpatrick, D. D. Duncan, E. M. Wells-Gray, *Opt. Lett.* **2008**, *33*, 2886.
- [111] H. Li, Z. Yu, Q. Zhao, Y. Luo, S. Cheng, T. Zhong, C. M. Woo, H. Liu, L. V. Wang, Y. Zheng, P. La, *Photonics Res.* **2023**, *11*, 631.
- [112] O. Thompson, M. Andrews, E. Hirst, *Biomed. Opt. Express* **2011**, *2*, 1021.
- [113] K. Basak, M. Manjunatha, P. K. Dutta, *Med. Biol. Eng. Comput.* **2012**, *50*, 547.
- [114] C. P. Valdes, H. M. Varma, A. K. Kristoffersen, T. Dragojevic, J. P. Culver, T. Durduran, *Biomed. Opt. Express* **2014**, *5*, 2769.
- [115] J. Qiu, Y. Li, Q. Huang, Y. Wang, P. Li, *Opt. Express* **2013**, *21*, 28902.
- [116] A. Rege, J. Senarathna, N. Li, N. V. Thakor, *IEEE Trans. Biomed. Eng.* **2012**, *59*, 1272.
- [117] J. Qiu, P. Li, W. Luo, J. Wang, H. Zhang, Q. Luo, *J. Biomed. Opt.* **2010**, *15*, 16003.
- [118] N. Li, X. Jia, K. Murari, R. Parlapalli, A. Rege, N. V. Thakor, *J. Neurosci. Methods* **2009**, *176*, 230.
- [119] J. Xu, A. K. Jahromi, C. Yang, *APL Photonics* **2021**, *6*, 016105.
- [120] A. G. Olmos, Z. Humlesen, V. Matchkov, D. D. Postnov, *Biomed. Opt. Expr.* **2023**, *14*, 1355.
- [121] A. Sdobnov, A. Bykov, G. Molodij, V. Kalchenko, T. Jarvinen, A. Popov, K. Kordas, I. Meglinski, *J. Phys. D: Appl. Phys.* **2018**, *51*, 155401.
- [122] P. Zakharov, A. Völker, A. Buck, B. Weber, F. Scheffold, *Opt. Lett.* **2006**, *31*, 3465.
- [123] S. Yuan, *Ph.D. Thesis*, Tufts University, Medford **2008**.
- [124] P. Li, S. Ni, L. Zhang, S. Zeng, Q. Luo, *Opt. Lett.* **2006**, *31*, 1824.
- [125] P. Zakharov, A. C. Völker, M. T. Wyss, F. Haiss, N. Calcinaghi, C. Zunzunegui, A. Buck, F. Scheffold, B. Weber, *Opt. Express* **2009**, *17*, 13904.
- [126] S. M. S. Kazmi, L. M. Richards, C. J. Schrandt, M. A. Davis, A. K. Dunn, *J. Cereb. Blood Flow Metab.* **2015**, *35*, 1076.
- [127] A. Nadort, R. G. Woolthuis, T. G. van Leeuwen, D. J. Faber, *Biomed. Opt. Express* **2013**, *4*, 2347.
- [128] A. B. Parthasarathy, S. M. S. Kazmi, A. K. Dunn, *Biomed. Opt. Express* **2010**, *1*, 246.
- [129] S. M. S. Kazmi, S. Balial, A. K. Dunn, *Biomed. Opt. Express* **2014**, *5*, 2157.
- [130] T. B. Rice, E. Kwan, C. K. Hayakawa, A. J. Durkin, B. Choi, B. J. Tromberg, *Biomed. Opt. Express* **2013**, *4*, 2880.
- [131] A. C. Völker, P. Zakharov, B. Weber, F. Buck, F. Scheffold, *Opt. Express* **2005**, *13*, 9782.
- [132] M. Medebach, N. Freiberger, O. Glatter, *Rev. Sci. Instrum.* **2008**, *79*, 73907.
- [133] C. Haro-Pérez, G. J. Ojeda-Mendoza, L. F. Rojas-Ochoa, *J. Chem. Phys.* **2011**, *134*, 244902.
- [134] A. Sdobnov, V. V. Kalchenko, A. V. Bykov, A. P. Popov, G. Molodij, I. Meglinski, *Opt. Spectros.* **2020**, *128*, 773.
- [135] S. Haleh, G. Hirc, P. Frederic, *J. Biomed. Opt.* **2017**, *22*, 10503.
- [136] J.-H. Park, W. Sun, M. Cui, *Proc. Natl. Acad. Sci. U. S. A.* **2015**, *112*, 9236.
- [137] A. Nadort, K. Kalkman, T. G. van Leeuwen, D. J. Faber, *Sci. Rep.* **2016**, *6*, 25258.
- [138] G. Nilsson, G. Salerud, T. Strömberg, K. Wårdell, M. Larsson, in *Biomedical Photonics Handbook*, 1st ed., CRC Press, Boca Raton, FL **2003**.
- [139] A. Humeau, W. Steenbergen, H. Nilsson, T. Strömberg, *Med. Biol. Eng. Comput.* **2007**, *45*, 421.
- [140] M. Leahy, *Microcirculation Imaging*, John Wiley & Sons, Hoboken, NJ **2012**.
- [141] I. V. Meglinski, S. J. Matcher, *Med. Biol. Eng. Comput.* **2001**, *39*, 44.
- [142] E. A. Zherebtsov, A. I. Zherebtsova, A. Doronin, A. V. Dunaev, K. V. Podmasteryev, A. Bykov, I. Meglinski, *J. Biomed. Opt.* **2017**, *22*, 40502.
- [143] I. M. Braverman, A. Keh, D. Goldminz, *J. Invest. Dermatol.* **1990**, *95*, 283.
- [144] E. Zherebtsov, I. Kozlov, V. Dremin, A. Bykov, A. Dunaev, I. Meglinski, *IEEE Trans. Biomed. Eng.* **2023**, *70*, 3.
- [145] G. Molodij, A. Sdobnov, Y. Kuznetsov, A. Harmelin, I. Meglinski, V. Kalchenko, *Phys. Med. Biol.* **2020**, *65*, 075007.
- [146] V. Dremin, E. Zherebtsov, A. Bykov, A. Popov, A. Doronin, I. Meglinski, *Appl. Opt.* **2019**, *58*, 9398.
- [147] Y. A. Abdulhameed, G. Lancaster, P. V. E. McClintock, A. Stefanovska, *Physiol. Meas.* **2019**, *40*, 074005.
- [148] H. He, Y. Tang, F. Zhou, J. Wang, Q. Luo, P. Li, *Opt. Lett.* **2012**, *37*, 3774.
- [149] M. A. Davis, S. M. S. Kazmi, A. K. Dunn, *J. Biomed. Opt.* **2014**, *19*, 86001.
- [150] E. Zherebtsov, V. Dremin, A. Popov, A. Doronin, D. Kurakina, M. Kirillin, I. Meglinski, A. Bykov, *Biomed. Opt. Express* **2019**, *10*, 3545.
- [151] I. V. Meglinski, V. V. Kal'chenko, Y. L. Kuznetsov, B. I. Kuznik, V. V. Tuchin, *Dokl. Phys.* **2013**, *58*, 323.
- [152] A. Sdobnov, A. Bykov, G. Molodij, V. Kalchenko, T. Jarvinen, A. Popov, K. Kordas, I. Meglinski, *J. Phys. D: Appl. Phys.* **2018**, *51*, 155401.
- [153] C. J. Pedersen, D. Huang, M. A. Shure, A. M. Rollins, *Opt. Lett.* **2007**, *32*, 506.
- [154] N. McDicken, A. Thomson, A. White, I. Toor, G. Gray, C. Moran, R. J. Watson, T. Anderson, *Echo Res. Pract.* **2019**, *6*, 105.
- [155] S. Xu, X. Yang, W. Liu, J. Jönsson, R. Qian, P. C. Konda, K. C. Zhou, L. Kreiß, H. Wang, Q. Dai, E. Berrocal, R. Horstmeyer, *Adv. Sci.* **2022**, *9*, 2201885.
- [156] D. D. Postnov, J. Tang, S. E. Erdener, K. Kılıç, D. A. Boas, *Sci. Adv.* **2020**, *6*, eabc4628.
- [157] E. Du, S. Shen, S. P. Chong, N. Chen, *Biomed. Opt. Express* **2020**, *11*, 2007.
- [158] M. M. Qureshi, Y. Liu, K. D. Mac, M. Kim, A. M. Safi, E. Chung, *Optica* **2021**, *8*, 1326.
- [159] M. M. Wu, K. Perdue, S.-T. Chan, K. A. Stephens, B. Deng, M. A. Franceschini, S. A. Carp, *Biomed. Opt. Express* **2022**, *13*, 1131.
- [160] W. Liu, R. Qian, S. Xu, P. Chandra Konda, J. Jönsson, M. Harfouche, D. Borycki, C. Cooke, E. Berrocal, Q. Dai, W. Haoqian, H. Roarke, *APL Photonics* **2021**, *6*, 026106.
- [161] E. J. Sie, H. Chen, E.-F. Saung, R. Catoen, T. Tietcke, M. A. Chevillet, F. Marsili, *Neurophotonics* **2020**, *7*, 035010.
- [162] M. B. Robinson, D. A. Boas, S. Sakadzic, M. A. Franceschini, S. A. Carp, *J. Biomed. Opt.* **2020**, *25*, 097004.
- [163] W. Zhou, O. Kholiqov, J. Zhu, M. Zhao, L. L. Zimmermann, R. M. Martin, B. G. Lyeth, V. J. Srinivasan, *Sci. Adv.* **2021**, *7*, eabe0150.
- [164] E. James, S. Powell, *Biomed. Opt. Express* **2020**, *11*, 6755.

- [165] J. Xu, A. K. Jahromi, J. Brake, J. E. Robinson, C. Yang, *APL Photonics* **2020**, *5*, 126102.
- [166] W. Zhou, M. Zhao, O. Kholiqov, V. J. Srinivasan, *Opt. Lett.* **2021**, *46*, 4498.
- [167] M. B. Robinson, S. A. Carp, A. Peruch, D. A. Boas, M. A. Franceschini, S. Sakadžić, *Biomed. Opt. Express* **2020**, *11*, 3071.
- [168] J. Sutin, B. Zimmerman, D. Tzulmankov, D. Tamborini, K. C. Wu, J. Selb, A. Gulinatti, I. Rech, A. Tosi, D. A. Boas, M. A. Franceschini, *Optica* **2016**, *3*, 1006.
- [169] A. M. Safi, S. Moka, M. Harrah, S. Cini, A. B. Parthasarathy, in *Optics and the Brain*, Optica Publishing Group, Washington, D.C **2021**, pp. BTh1B–6.
- [170] S. A. Carp, D. Tamborini, D. Mazumder, K.-C. Wu, M. R. Robinson, K. A. Stephens, O. Shatrovov, N. Lue, N. Ozana, M. H. Blackwell, M. A. Franceschini, *J. Biomed. Opt.* **2020**, *25*, 097003.
- [171] M. Z. Ansari, E.-J. Kang, M. D. Manole, J. P. Dreier, A. Humeau-Heurtier, *Microvasc. Res.* **2017**, *111*, 49.
- [172] J. He, H. Lu, L. Young, R. Deng, D. Callow, S. Tong, X. Jia, *J. Cereb. Blood Flow Metab.* **2019**, *39*, 1161.
- [173] X. Jia, J. He, H. Lu, L. Young, S. Tong, *Ann. Phys. Rehabil. Med.* **2018**, *61*, e425.
- [174] L. Yin, T. Yu, L. Cheng, X. Liu, W. Zhang, H. Zhang, L. Du, W. He, *BMC neuroscience* **2022**, *23*, 80.
- [175] P. Hu, B. Niu, H. Yang, Y. Xia, D. Chen, C. Meng, K. Chen, B. Biswal, *Microcirculation* **2022**, *29*, e12783.
- [176] A. N. Pavlov, A. S. Abdurashitov, A. A. Koronovskii Jr, O. N. Pavlova, O. V. Semyachkina-Glushkovskaya, J. Kurths, *Commun. Nonlinear Sci. Numer. Simul.* **2020**, *85*, 105232.
- [177] K. Venugopal, S. N. Unni, A. Bach, C. Conzen, U. Lindauer, *J. Biophotonics* **2019**, *12*, 201800408.
- [178] P. Cumsille, E. Lara, P. Verdugo-Hernández, J. Acurio, C. Escudero, *Microvasc. Res.* **2022**, *144*, 104418.
- [179] S. Uchida, F. Kagitani, *J. Physiol. Sci.* **2018**, *68*, 415.
- [180] C. Crouzet, R. H. Wilson, A. Bazrafkan, M. H. Farahabadi, D. Lee, J. Alcocer, B. J. Tromberg, B. Choi, Y. Akbari, *Biomed. Opt. Express* **2016**, *7*, 4660.
- [181] R. H. Wilson, C. Crouzet, M. Torabzadeh, A. K. Bazrafkan, M. Hosseini-Farahabadi, B. Jamasian, D. Donga, J. Alcocer, S. M. Zaher, B. Choi, Y. Akbari, B. J. Tromberg, *Neurophotonics* **2017**, *4*, 045008.
- [182] R. H. Wilson, C. Crouzet, M. Torabzadeh, A. Bazrafkan, N. Maki, B. J. Tromberg, Y. Akbari, B. Choi, *Neurophotonics* **2021**, *8*, 025001.
- [183] Y. Zhao, K. Wang, W. Li, H. Zhang, Z. Qian, Y. Liu, *J. Biomed. Opt.* **2020**, *25*, 056005.
- [184] A. Mangraviti, F. Volpin, J. Cha, S. I. Cunningham, K. Raje, M. J. Brooke, H. Brem, A. Olivi, J. Huang, B. M. Tyler, A. Rege, *Sci. Rep.* **2020**, *10*, 7614.
- [185] B. Liu, S. Shah, G. Küreli, A. Devor, D. A. Boas, X. Cheng, *Biomed. Opt. Express* **2023**, *14*, 4790.
- [186] G. Pivachenko, I. Kozlov, V. Dremine, D. Stavtsev, E. Seryogina, K. Kandurova, V. Shupletsov, K. Lapin, A. Alekseyev, S. Kuznetsov, A. Bykov, A. Dunaev, I. Meglinski, *J. Biophotonics* **2021**, *14*, 202100216.
- [187] V. Kalchenko, A. Sdobnov, I. Meglinski, Y. Kuznetsov, G. Molodij, A. Harmelin, *Photonics* **2019**, *6*, 80.
- [188] V. Kalchenko, Y. Kuznetsov, A. Harmelin, I. V. Meglinski, *J. Biomed. Opt.* **2012**, *17*, 50502.
- [189] V. Kalchenko, Y. L. Kuznetsov, I. Meglinski, *Quantum Electron.* **2013**, *43*, 679.
- [190] V. Kalchenko, Y. Kuznetsov, D. Preise, I. V. Meglinski, A. Harmelin, *J. Biomed. Opt.* **2014**, *19*, 60502.
- [191] V. Kalchenko, K. Ziv, Y. Addadi, N. Madar-Balakirski, I. Meglinski, M. Neeman, A. Harmelin, *Laser Phys. Lett.* **2010**, *7*, 603.
- [192] L. M. Richards, S. M. S. Kazmi, K. E. Olin, J. S. Waldron, D. J. Fox Jr, A. K. Dunn, *J. Cereb. Blood Flow Metab.* **2017**, *37*, 3097.
- [193] D. R. Miller, R. Ashour, C. T. Sullender, A. K. Dunn, *Neurophotonics* **2022**, *9*, 021908.
- [194] S. Tao, T. Zhang, K. Zhou, X. Liu, Y. Feng, W. Zhao, J. Chen, *Front. Surg.* **2022**, *9*, 855397.
- [195] Y. Guo, Y. Weng, Y. Zhang, S. Tong, Y. Liu, Z. Lu, P. Miao, *Biomed. Opt. Express* **2023**, *14*, 1480.
- [196] M. Ideguchi, K. Kajiwara, K. Yoshikawa, H. Goto, K. Sugimoto, T. Inoue, S. Nomura, M. Suzuki, *J. Neurosurg.* **2017**, *126*, 274.
- [197] Z. Kalyuzhner, S. Agdarov, I. Orr, Y. Beiderman, A. Bennett, Z. Zalevsky, *Sci. Rep.* **2022**, *12*, 519.
- [198] B. Kim, S. Zilpelwar, E. J. Sie, F. Marsili, B. Zimmermann, D. A. Boas, X. Cheng, *Commun. Biol.* **2023**, *6*, 844.
- [199] B. B. Shih, D. Allan, F. R. De Grujil, L. E. Rhodes, *J. Invest. Dermatol.* **2015**, *135*, 1197.
- [200] M. Elmasry, R. Mirdell, E. Tesselaar, S. Farnebo, F. Sjöberg, I. Steinvall, *Burns* **2019**, *45*, 798.
- [201] S. Barsotti, A. D'Ascanio, V. Valentina, S. Chiara, B. Silvia, A. Laura, M. Mosca, A. Della Rossa, *Clin. Rheumatol.* **2020**, *39*, 69.
- [202] C. D. Nguyen, J. Hult, R. Sheikh, K. Tenland, U. Dahlstrand, S. Lindstedt, M. Malmjö, *Ophthalmic Plast. Reconstr. Surg.* **2018**, *34*, 361.
- [203] B. Yang, O. Yang, J. Guzman, P. Nguyen, C. Crouzet, K. E. Osann, K. M. Kelly, J. S. Nelson, B. Choi, *Lasers Surg. Med.* **2015**, *47*, 469.
- [204] A. Lazaridis, A. Triantafyllou, K. Dipla, P. Dolgyras, N. Koletsos, P. Anyfanti, S. Aslanidis, S. Douma, E. Gkaliagkousi, *Hypertens. Res.* **2022**, *45*, 445.
- [205] C. Linkous, A. D. Pagan, C. Shope, L. Andrews, A. Snyder, T. Ye, M. Valdebran, *JID Innovations* **2023**, *3*, 100187.
- [206] G. Guven, A. Dijkstra, T. M. Kuijper, N. Trommel, M. E. van Baar, A. Topeli, C. Ince, C. H. van der Vlies, *Microcirculation* **2023**, *30*, 12795.
- [207] D.-Y. Li, Q. Xia, T.-T. Yu, J.-T. Zhu, D. Zhu, *Light: Sci. Appl.* **2021**, *10*, 241.
- [208] R. Mirdell, S. Farnebo, F. Sjöberg, E. Tesselaar, *Burns* **2019**, *45*, 1325.
- [209] R. Mirdell, S. Farnebo, F. Sjöberg, E. Tesselaar, *Burns* **2018**, *44*, 90.
- [210] M. J. Schaap, A. Chizari, T. Knop, H. M. Groenewoud, P. E. van Erp, E. M. de Jong, W. Steenbergen, M. M. Seyger, *Skin Res. Technol.* **2022**, *28*, 104.
- [211] A. Margouta, P. Anyfanti, A. Lazaridis, B. Nikolaidou, K. Mastrogiannis, A. Malliara, A. Patsatsi, A. Triantafyllou, S. Douma, M. Doumas, E. Gkaliagkousi, *Life* **2022**, *12*, 1796.
- [212] A. Couturier, R. Bouvet, J.-L. Cracowski, M. Roustit, *Microvasc. Res.* **2022**, *141*, 104319.
- [213] C. P. Denton, D. Khanna, *Lancet* **2017**, *390*, 1685.
- [214] B. Ruaro, A. Sulli, V. Smith, S. Paolino, C. Pizzorni, M. Cutolo, *Microvasc. Res.* **2015**, *101*, 82.
- [215] B. Ruaro, A. Sulli, C. Pizzorni, S. Paolino, V. Smith, E. Alessandri, A. C. Trombetta, J. Alsheyyab, M. Cutolo, *Microvasc. Res.* **2018**, *115*, 28.
- [216] O. A. Mennes, J. J. Van Netten, J. G. Van Baal, W. Steenbergen, *Physiol. Meas.* **2019**, *40*, 65002.
- [217] G. Varetto, F. Verzini, A. Trucco, E. Frola, F. Spalla, L. Gibello, M. Boero, G. Capaldi, P. Rispoli, *Ann. Vasc. Surg.* **2020**, *64*, 246.
- [218] C. D. Ansson, J. V. Berggren, K. Tenland, R. Sheikh, J. Hult, U. Dahlstrand, S. Lindstedt, M. Malmjö, *Ophthalmic Plast. Reconstr. Surg.* **2020**, *36*, 481.
- [219] J. Berggren, N. Castelo, K. Tenland, U. Dahlstrand, K. Engelsberg, S. Lindstedt, R. Sheikh, M. Malmjö, *Ophthalmic Plast. Reconstr. Surg.* **2021**, *37*, 324.
- [220] J. V. Berggren, K. Tenland, R. Sheikh, J. Hult, K. Engelsberg, S. Lindstedt, M. Malmjö, *Ophthalmic Plast. Reconstr. Surg.* **2022**, *38*, 274.
- [221] J. Berggren, N. Castelo, K. Tenland, K. Engelsberg, U. Dahlstrand, J. Albinsson, R. Sheikh, S. Lindstedt, M. Malmjö, *Ophthalmic Plast. Reconstr. Surg.* **2021**, *37*, 269.

- [222] A. H. Wiktorin, J. V. Berggren, M. Malmjö, S. Lindstedt, R. Sheikh, E. Bohman, *Ophthalmic Plast. Reconstr. Surg.* **2022**, *38*, 588.
- [223] L. Engqvist, R. Sheikh, U. Dahlstrand, *J. Pediatr. Ophthalmol. Strabismus* **2022**, *26*, 155.
- [224] J. Bunke, A. Merdasa, M. Stridh, P. Rosenquist, J. Berggren, J. E. Hernandez-Palacios, U. Dahlstrand, N. Reistad, R. Sheikh, M. Malmjö, *Ophthalmic Plast. Reconstr. Surg.* **2022**, *38*, 462.
- [225] H. Ghahvehchian, M. B. Kashkouli, N. Karimi, *Ophthalmic Plast. Reconstr. Surg.* **2023**, *39*, 99.
- [226] C. Chen, M. Zhang, N. Yu, W. Zhang, X. Long, Y. Wang, X. Wang, *Lasers Surg. Med.* **2021**, *53*, 865.
- [227] S. Li, H. Wang, Y. Xiao, M. Zhang, N. Yu, A. Zeng, X. Wang, *J. Pers. Med.* **2022**, *12*, 981.
- [228] D. Zhu, K. V. Larin, Q. Luo, V. V. Tuchin, *Laser Photonics Rev.* **2013**, *7*, 732.
- [229] J. Wang, N. Ma, R. Shi, Y. Zhang, T. Yu, D. Zhu, *IEEE J. Sel. Top. Quantum Electron.* **2013**, *20*, 256.
- [230] C. Zhang, W. Feng, Y. Zhao, T. Yu, P. Li, T. Xu, Q. Luo, D. Zhu, *Theranostics* **2018**, *8*, 2696.
- [231] V. Kalchenko, D. Israeli, Y. Kuznetsov, I. Meglinski, A. Harmelin, *J. Biophotonics* **2015**, *8*, 897.
- [232] V. Kalchenko, I. Meglinski, A. Sdobnov, Y. Kuznetsov, A. Harmelin, *J. Biomed. Opt.* **2019**, *24*, 60501.
- [233] J. Guilbert, M. Desjardins, *J. Biophotonics* **2022**, *15*, 202100218.
- [234] B. Lertsakdadet, B. Y. Yang, C. E. Dunn, A. Ponticorvo, C. Crouzet, N. Bernal, A. J. Durkin, B. Choi, *J. Biomed. Opt.* **2018**, *23*, 36006.
- [235] B. Lertsakdadet, C. Dunn, A. Bahani, C. Crouzet, B. Choi, *Biomed. Opt. Express* **2019**, *10*, 5149.
- [236] K. W. Walek, S. Stefan, J.-H. Lee, P. Puttigampala, A. H. Kim, S. W. Park, P. J. Marchand, F. Lesage, T. Liu, Y.-W. A. Huang, D. A. Boas, C. Moore, J. Lee, *Nat. Commun.* **2023**, *14*, 2982.
- [237] J. Torres, L. Torner, *Twisted Photons: Applications of Light with Orbital Angular Momentum*, Wiley-VCH Verlag GmbH, Weinheim, Germany **2011**.
- [238] A. Konovalov, V. Gadzhiagaev, F. Grebenev, D. Stavtsev, G. Piavchenko, A. Gerasimenko, D. Telyshev, I. Meglinski, S. Eliava, *World Neurosurg.* **2023**, *171*, 35.



Anton Sdobnov is a post-doctoral researcher at the Opto-Electronics and Measurement Techniques Unit (OPEM), University of Oulu, Finland. In 2021, Anton received a Ph.D. degree in physics at Saratov State University, Russia. In 2022, he received a D.Sc. degree in technology at the University of Oulu, Finland. His scientific interests are in the areas of non-invasive biomedical imaging, tissue optical clearing, and vortex light propagation in scattering media.



Gennadii Piavchenko received his MD in Neurology, Ph.D. in Cellular Biology, and M.Sc. in Pedagogics. He is an Associate Professor at the Human Anatomy and Histology Department at Sechenov First Moscow State Medical University, Moscow. His research interests primarily revolve around the development and practical implementation of interdisciplinary approaches that integrate behavioral neuroscience and applied pharmacology with emerging trends in biophotonics.



Alexander Bykov is an Adjunct Professor (Docent) in biophotonics and sensors technologies at the Opto-Electronics and Measurement Techniques Unit (OPEM), University of Oulu, Finland. In 2010, he received his D.Sc. (Tech.) degree. Since 2019, he has been the leader of the Biophotonics Group at OPEM. His scientific interests are in the areas of non-invasive optical diagnostics of biotissues, the theory of light propagation in scattering media, and numerical simulation of light transport. He is a senior member of Optica.



Igor Meglinski is a Professor in Quantum Biophotonics and Biomedical Engineering at the College of Engineering and Physical Sciences at Aston University (UK). His research interests lie at the interface between physics, optics, and biomedical engineering, focusing on the development of new non-invasive imaging/diagnostic techniques and their application in medicine & biology, pharmacy, environmental monitoring, food sciences and health care industries. He is a Chartered Physicist (CPhys) and Chartered Engineer (CEng), Senior Member of IEEE, Fellow of Institute of Physics, FRMS, Fellow SPIE, and Fellow OPTICA (formerly Optical Society of America).